

Research Paper

Low-frequency integrated radio spectra of diffuse, steep-spectrum sources in galaxy clusters: palaeontology with the MWA and ASKAP

S. W. Duchesne^{1,*}, M. Johnston-Hollitt^{1,2}, and I. Bartalucci³

¹International Centre for Radio Astronomy Research (ICRAR), Curtin University, Bentley, WA 6102, Australia

²Curtin Institute for Computation, Curtin University, GPO Box U1987, Perth, WA 6845, Australia

³INAF - Istituto di Astrofisica Spaziale e Fisica Cosmica di Milano, Via A. Corti 12, 20133 Milano, Italy

Abstract

Galaxy clusters have been found to host a range of diffuse, non-thermal emission components, generally with steep, power law spectra. In this work we report on the detection and follow-up of radio halos, relics, remnant radio galaxies, and other fossil radio plasmas in Southern Sky galaxy clusters using the Murchison Widefield Array and the Australian Square Kilometre Array Pathfinder. We make use of the frequency coverage between the two radio interferometers—from 88 to ~ 900 MHz—to characterise the integrated spectra of these sources within this frequency range. Highlights from the sample include the detection of a double relic system in Abell 3186, a mini-halo in RXC J0137.2–0912, a candidate halo and relic in Abell 3399, and a complex multi-episodic head-tail radio galaxy in Abell 3164. We compare this selection of sources and candidates to the literature sample, finding sources consistent with established radio power–cluster mass scaling relations. Finally, we use the low-frequency integrated spectral index, α ($S_\nu \propto \nu^\alpha$), of the detected sample of cluster remnants and fossil sources to compare with samples of known halos, relics, remnants and fossils to investigate a possible link between their electron populations. We find the distributions of α to be consistent with relic and halo emission generated by seed electrons that originated in fossil or remnant sources. However, the present sample sizes are insufficient to rule out other scenarios.

Keywords: galaxies: clusters: general – large-scale structure of the Universe – radio continuum: general – X-rays: galaxies: clusters

1. Introduction

Clusters of galaxies are formed through often highly energetic merger events and accretion from filaments of the Cosmic Web. Clusters are comprised of constituent galaxies, X-ray emitting plasmas, and $\sim \mu\text{G}$ -level magnetic fields (Clarke et al., 2001; Johnston-Hollitt, 2003). In a fraction of clusters, large-scale (~ 1 Mpc) steep-spectrum ($\alpha \lesssim -1$ ¹), diffuse radio emission is observed as centrally-located radio *halos* and peripherally-located radio *relics* (see van Weeren et al., 2019, and references therein). These large-scale synchrotron-emitting sources are not thought to be presently fuelled by active galactic nuclei (AGN), rather they are assumed to be generated through in situ (re-)acceleration of particles (e.g. Jaffe, 1977; Enßlin et al., 1998). Such sources are observed in predominantly merging, or otherwise morphologically disturbed clusters (e.g. Buote, 2001; Brunetti et al., 2009; Cassano et al., 2010; Botteon et al., 2018; Golovich et al., 2019).

Radio *halos* are generally spatially correlated with the thermal, X-ray-emitting core of the cluster and are observed with morphologies ranging from circular (e.g. Orrú et al., 2007; Murgia et al., 2009) to more complex and elongated structures (e.g. van Weeren et al., 2012). Radio halos are generally observed to have power law spectra, though some halos with significant spectral coverage show steepening beyond GHz frequencies (Thierbach et al., 2003; Xie et al., 2020; Rajpurohit et al., 2021c). Merger-driven turbulence in

the ICM may provide a mechanism for in situ (re-)acceleration of seed particles from either the thermal pool of electrons or from a pre-accelerated population of mildly-relativistic ‘fossil’ electrons throughout the cluster volume (e.g. Brunetti et al., 2001; Buote, 2001; Brunetti & Jones, 2014).

Radio *relics* occur in the low-density cluster outskirts, where strong shocks in the intra-cluster medium (ICM) are thought to (re-)accelerate electrons through diffusive-shock acceleration (DSA; e.g. Enßlin et al. 1998, and similar processes; e.g. Kang 2015) either originating a ‘fossil’ electron population (e.g. Markevitch et al., 2005; Kang & Ryu, 2011, 2016) or accelerated from the thermal pool of electrons in the cluster (e.g. Enßlin et al., 1998; Hoeft & Brüggen, 2007). Unlike radio halos, relics are often observed with highly ordered, linearly polarized emission (e.g. Johnston-Hollitt, 2003; van Weeren et al., 2010; Pearce et al., 2017). The integrated spectra of relics are generally power laws (e.g. Hindson et al., 2014; Loi et al., 2017; Rajpurohit et al., 2020; Duchesne et al., 2021a), though few examples exist with curvature beyond GHz frequencies (e.g. Trasatti et al., 2015). In some cases, radio relics have been observed to be located co-spatially with X-ray shocks/surface brightness discontinuities (e.g. Finoguenov et al., 2010; Botteon et al., 2016a; Botteon et al., 2016b).

Along with the large-scale radio halos and relics, other diffuse, non-thermal sources have been observed in clusters with many observational and physical similarities (see e.g. van Weeren et al., 2019, for a review of source types and nomenclature). Radio *mini-halos* are $\lesssim 500$ kpc synchrotron-emitting regions surrounding

*stefan.duchesne.astro@gmail.com

¹Where α is defined via $S_\nu \propto \nu^\alpha$.

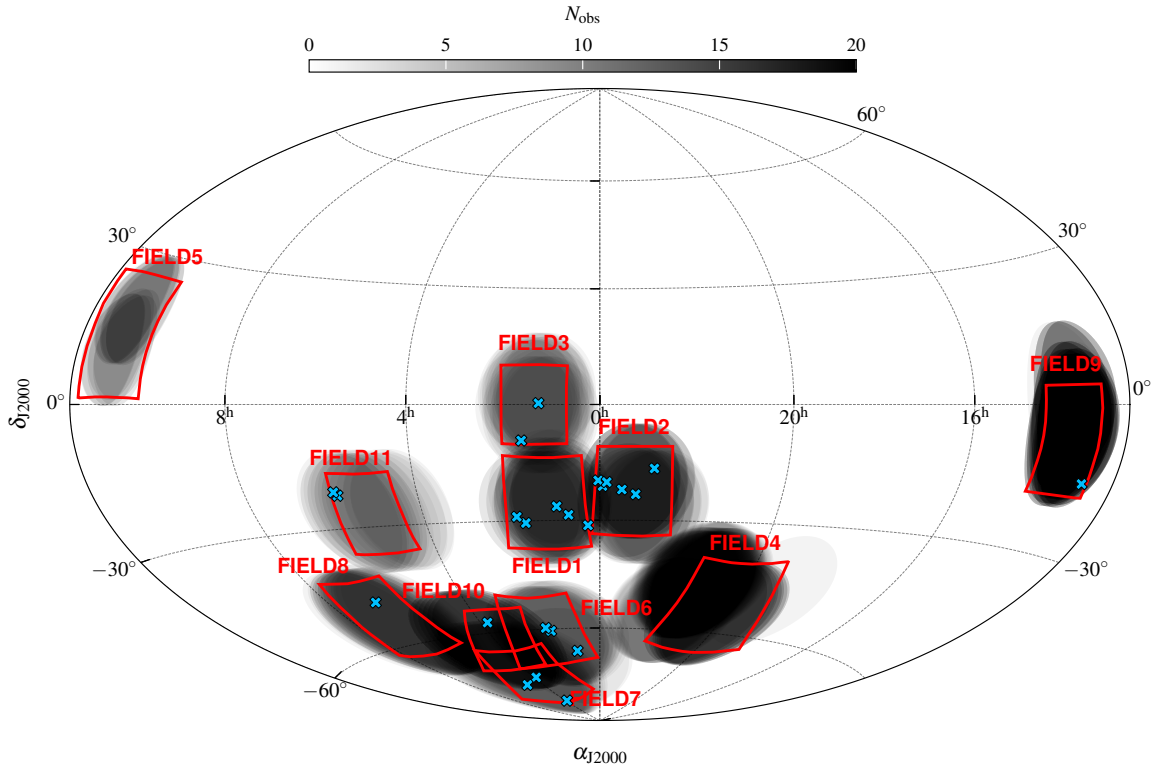


Figure 1. The sky coverage of the MWA-2 diffuse source follow-up survey, with named fields labelled and cluster targets reported in this work noted as blue ‘x’ marks. Actual MWA-2 pointings at 154 MHz are shown as transparent black circles, indicating relative sensitivity of fields. While no sources from either FIELD4 or FIELD5 are reported in this work (as discussed in the text) we show their locations for completeness.

AGN in the centres of some cool-core (CC) clusters (see e.g. Bravi et al., 2016; Giacintucci et al., 2019). Observationally, they appear as small radio halos with similar spectral and morphological properties but are thought to form via re-acceleration of AGN outflow from small-scale turbulence and sloshing within the cluster core (e.g. Gitti et al., 2002). Mini-halos are not typically associated with major mergers.

Beyond the cluster core, smaller-scale relic-like sources of various types are also found: radio *phoenixes* or otherwise revived *fossil* sources have been observed (e.g. Slee et al., 2001; Cohen & Clarke, 2011; Giacintucci et al., 2020; Hodgson et al., 2021). These sources are typically on the order of a few hundred kpc in size and vary morphologically. They range from ultra-steep spectrum fossil plasmas that have possibly been revived via shock-driven adiabatic compression (e.g. Enßlin & Gopal-Krishna, 2001; Enßlin & Brüggen, 2002), radio galaxies with shocks passing through an outer lobe/tail, re-energising the radio plasma (e.g. gentle re-energisation; de Gasperin et al. 2017, or less-gentle processes; Bonafede et al. 2014; van Weeren et al. 2017), to true remnant radio galaxies with no evidence of re-energisation and are simply fading from normal energy losses after their AGN have switched off or have entered a low-power state (e.g. Parma et al., 2007; Murgia et al., 2011). Distinguishing between what are effectively radio galaxies at various stages through their life-cycle is difficult and in the case of radio phoenixes often the hosting cluster does not show evidence of merger-driven shocks. Finally, in rare cases

synchrotron-emitting bridges have been observed between cluster pairs (e.g. Govoni et al., 2019; Botteon et al., 2020a), likely formed through turbulence in the inter-cluster region (Brunetti & Vazza, 2020).

It is not yet clear whether the seed electrons responsible for radio halos and relics are from the thermal pool or from fossils that have diffused into the surrounding ICM—observations of spectra of such sources are beginning to provide answers (e.g. Rajpurohit et al., 2021c,b,a). The current generation of radio interferometers, including the Murchison Widefield Array (MWA; Tingay et al., 2013; Wayth et al., 2018), the Australian Square Kilometre Array Pathfinder (ASKAP; Hotan et al., 2021), the LOw Frequency ARray (LOFAR; van Haarlem et al., 2013), and MeerKAT² (Jonas & MeerKAT Team, 2016) are beginning to uncover diffuse cluster sources at higher rates (e.g. Wilber et al., 2020; Duchesne et al., 2020; Di Gennaro et al., 2021; Brüggen et al., 2021; van Weeren et al., 2021; Knowles et al., 2021; Duchesne et al., 2021a; Hodgson et al., 2021; Duchesne et al., 2021b,c), providing unprecedented insight into cluster diffuse source populations, paving the way for future observations with the Square Kilometre Array (SKA). In this work we detail a targeted campaign to follow-up diffuse radio emission in clusters originally detected in MWA surveys, leveraging the wide bandwidth of the MWA to investigate the low-frequency integrated spectra of these sources.

Throughout this paper, we assume a standard Λ Cold Dark

²Karoo Array Telescope

Matter cosmology with $H_0 = 70 \text{ km s}^{-1} \text{ Mpc}^{-1}$, $\Omega_M = 0.3$, and $\Omega_\Lambda = 1 - \Omega_M$. Unless otherwise stated, frequency subscripts and superscripts on quantities are in units of MHz.

2. Data & methods

2.1. Cluster sample

Duchesne et al. (2021b, hereafter D21) report a number of candidate diffuse cluster sources detected in a large, deep $45^\circ \times 45^\circ$ MWA image created for foreground modelling of the Epoch of Re-ionization 0-h field (Offringa et al., 2016). Due to the low resolution of the MWA, many of these sources had an uncertain nature. With the upgrade to the Phase 2 ‘extended’ MWA (Wayth et al., 2018, hereafter MWA-2) and the allure of an increase in resolution by a factor of two, we carried out re-observation of a selection of these sources as part of MWA project G0045 with Director’s Time observations of two additional fields and the addition of overlapping archival observations.

At the same time, a candidate list of diffuse cluster sources had been prepared based on visual searches of the GaLactic and Extragalactic MWA (GLEAM) survey (Wayth et al., 2015; Hurley-Walker et al., 2017). These searches focused on clusters from the Meta-Catalogue of X-ray detected Clusters (MCXC; Piffaretti et al., 2011), the Abell catalogues (Abell, 1958; Abell et al., 1989), *Planck* Sunyaev–Zel’dovich clusters (Planck Collaboration et al., 2015, 2016), and a handful of miscellaneous clusters serendipitously found to host candidate diffuse emission that are nearby other clusters from the aforementioned catalogues. While the full sample is not within the scope of this work (it would be prohibitive to perform targeted follow-up of close to 200 sources), we present here 31 sources across 9 fields³. Due to the large field of view of the MWA (~ 20 deg at 216 MHz and ~ 60 deg at 88 MHz) we planned MWA-2 observations to cover a total 22 clusters (Table 1). While the 200-MHz wideband GLEAM image is usually sufficient to detect and measure flux density of these sources, the lower-frequency bands become prohibitively confused for use here. The fields observed (labelled FIELD1–11) are shown on Fig. 1. FIELD5 and our target source within Abell 1127 were presented in Duchesne et al. (2020), while two sources from the current survey have already been reported: Abell 141 in FIELD1 and Abell 3404 in FIELD8 (Duchesne et al., 2021c). While generally we will not report non-detections (or more accurately, non-confirmations) from the non-public candidate list, we will, where available, report any such sources from D21 in Appendix A.

2.2. Observations with the MWA-2

For all fields, we observed a range of frequencies, mirroring the GLEAM survey frequency selections: 30-MHz instantaneous bandwidth observations centered on 88, 118, 154, 185, and 216 MHz. Observations are performed in the MWA-standard ‘snapshot’ observing mode, with 2-min drift-scan snapshots. Each snapshot is calibrated and imaged independently prior to stacking/mosaicking.

Processing of the MWA-2 data follow the recipe described in detail by Duchesne et al. (2020) making use of the purpose-built Phase II Pipeline (piip⁴) with constituent software which will be briefly described. Individual snapshots are retrieved from the Pawsey Supercomputing Centre⁵ archive using the MWA component of the All-Sky Virtual Observatory⁶ which performs general pre-processing and initial RFI flagging with AOFlagger⁷ (Offringa et al., 2015). After snapshots are retrieved and pre-processed, they are calibrated using an implementation of the *Mitchcal* algorithm (Offringa et al., 2016) using a global sky model as described in Duchesne et al. (2020). Imaging per snapshot is performed with WSClean⁸ (version 2.9.0; Offringa et al., 2014; Offringa & Smirnov, 2017) using multi-scale CLEANing.

Final images are corrected for astrometry using *fits_warp.py* (version 2.0; Hancock et al., 2018) and the flux scale is set using *flux_warp*⁹ (version 1.14). Both of these tools take an input sky model generated by cross-matching and spectral modelling of GLEAM, the NRAO¹⁰ VLA¹¹ Sky Survey (NVSS; Condon et al., 1998) and/or the Sydney University Molonglo Sky Survey (SUMSS; Bock et al., 1999; Mauch et al., 2003; Murphy et al., 2007) using the Positional Update and Matching Algorithm (PUMA; Line et al., 2017). This sky model is in turn cross-matched to point sources in the snapshot image catalogues to calculate astrometric offsets and flux density discrepancies. Corrections are applied over the snapshots via interpolation between cross-matched sources. Finally, snapshot images are stacked to create mosaics as described in Duchesne et al. (2020). Flux density scale uncertainties are derived by comparing point source flux densities with the PUMA-generated sky model finding ~ 2 –10 per cent standard deviation across the observed fields and frequencies. An additional 8 per cent is added in quadrature as inherited from the GLEAM survey, which dominates the flux densities in the sky model. Bulk image details are presented in Table 2.

The ‘extended’ configuration of the MWA was created with the same number of tiles (i.e. 128) as the Phase I MWA due to limitations of the current correlator. Creating the longer baselines of the MWA-2 therefore required removing a significant number of short baselines, reducing the sensitivity to larger angular scales compared to the Phase I MWA (Hodgson et al., 2020). While the loss of sensitivity for this work is comparatively minimal, we still find that images weighted with a ‘Briggs’ (Briggs, 1995) robust parameter of $\leq +0.5$ begin to significantly lose large-scale flux. Therefore, for flux density measurements we create a set of robust +2.0 images for all fields except FIELD11 for which we use robust +1.0¹². We also create images at 0.0 and +0.5 to leverage the

⁴<https://gitlab.com/Sunmish/piip>

⁵<https://pawsey.org.au/>

⁶<https://asvo.org.au/>

⁷<https://gitlab.com/aroffringa/aoflagger>

⁸<https://gitlab.com/aroffringa/wsclean>

⁹https://gitlab.com/Sunmish/flux_warp

¹⁰National Radio Astronomy Observatory

¹¹Very Large Array

¹²There is no functional difference between the robust +1.0 and +2.0 weighting for the MWA-2 data with respect to image resolution and sensitivity, however, the FIELD11 data were processed at an earlier date for a separate project while more recent data-processing is done at +2.0.

³A total of 11 fields were observed, 1 is presented in Duchesne et al. (2020), and one was not able to be processed.

Table 1 Clusters and sources discussed in this work.

Cluster	FIELD	α_{J2000}^1 (J2000)	δ_{J2000}^1 (J2000)	z	M_{500}^2 ($\times 10^{14} M_{\odot}$)	Type ³	Ref. ⁴
Abell 0122	1	00:57:24	-26:16:50	0.113	1.73	r/F	(a)/(e)/(c)/(d)
Abell 2751	1	00:16:20	-31:21:55	0.107	1.26	r/F	(a)/(b)/(c)/(d)
Abell 2811	1	00:42:09	-28:32:09	0.108	$3.67^{+0.35}_{-0.37}$	cH	(a)/(e)/(f)/(d)
Abell 2496	2	22:51:00	-16:24:24	0.123	$3.36^{+0.30}_{-0.32}$	r	(a)/(b)/(w)/(d)
Abell 2680	2	23:56:28	-21:02:18	0.190	$3.2^{+0.8}_{-1.0}$	cH	(a)/(h)/(i)/(d)
Abell 2693	2	00:02:10	-19:33:18	0.173	$2.1^{+0.5}_{-0.6}$	cH/p	(a)/(h)/(d)
Abell S1099	2	23:13:16	-23:08:40	0.110	-	r	(j)/(k)/(d)
AqrCC 087	2	23:31:30	-21:55:00	-	-	F	(k)/-/
RXC J2351.0-1954	2	23:51:07	-19:58:52	0.248	$5.60^{+0.59}_{-0.62}$	p, r/F, U	(l)/(l)/(f)/(d)
Abell 0168	3	01:15:12	+00:19:48	0.045	$1.87^{+0.29}_{-0.31}$	R	(a)/(b)/(f)/(m)
RXC J0137.2-0912	3	01:37:15	-09:12:10	0.039	0.95	mH, RG	(n)/(n)/(c)/-
Abell S0112	6	00:57:48	-66:48:44	0.067	1.62	F	(j)/(o)/(c)/-
MCXC J0145.2-6033	6	01:45:12	-60:33:45	0.180	$3.55^{+0.42}_{-0.44}$	cmH	(p)/(p)/(f)/-
MCXC J0154.2-5937	6	01:54:15	-59:39:38	0.360	1.41	cGRG	(q)/(q)/(c)/-
Abell 3186	7	03:52:30	-74:01:51	0.127	$6.44^{+0.24}_{-0.24}$	R, R, cH	(j)/(b)/(f)/-
Abell S0405	7	03:51:09	-82:13:00	0.061	$2.51^{+0.20}_{-0.21}$	r	(j)/(r)/(f)/-
PSZ1 G287.95-32.98	7	04:59:38	-75:47:48	0.250	$5.88^{+0.40}_{-0.41}$	cH	(f)/(s)/(f)/-
Abell 3399	8	06:37:19	-48:28:42	0.203	$4.81^{+0.37}_{-0.39}$	cR, cH	(j)/(t)/(f)/-
MCXC J1253.2-1522	9	12:53:14	-15:22:48	0.046 ⁵	0.98	F	(c)/(c)/(c)/-
Abell 3164	10	03:46:10	-57:03:00	0.059	$1.62^{+0.26}_{-0.28}$	F, F, F	(j)/(u)/(f)/-
Abell 3365	11	05:48:50	-21:54:43	0.093	1.66	R, U	(j)/(b)/(c)/(v)
Abell 0550	11	05:52:52	-21:03:25	0.099	$3.87^{+0.25}_{-0.27}$	r	(a)/(r)/(w)/-

¹ Coordinates are shown in units of hours, minutes, seconds, and degrees, arcminutes, arcseconds.

² Mass within R_{500} , the radius within which the mean density of the cluster is 500 times the critical density of the Universe.

³ Detected diffuse source types (either as reported in the literature or as determined in this work): relic (R), halo (H), mini-halo (mH), remnant radio galaxy/AGN (r), miscellaneous fossil plasma/re-accelerated fossil plasma source (e.g. phoenix) (F), candidate (c), point source (p), normal radio galaxy (RG), giant radio galaxy (GRG), unclassified (U).

⁴ References for position/ z / M_{500} /previously detected diffuse emission: (a) Abell (1958). (b) Struble & Rood (1999). (c) ($M_{X,500}$) Piffaretti et al. (2011). (d) Duchesne et al. (2021b). (e) Zaritsky et al. (2006). (f) ($M_{SZ,500}$) Planck Collaboration et al. (2015). (g) Cavagnolo et al. (2008). (h) Coziol et al. (2009). (i) Wen & Han (2015). (j) Abell et al. (1989). (k) Caretta et al. (2002). (l) Chon & Böhringer (2012). (m) Dwarakanath et al. (2018). (n) Cruddace et al. (2002). (o) Garilli et al. (1993). (p) Schwoppe et al. (2000). (q) Vikhlinin et al. (1998). (r) De Grandi et al. (1999). (s) Planck Collaboration et al. (2014). (t) Böhringer et al. (2004). (u) Fleenor et al. (2006). (v) van Weeren et al. (2011). (w) Planck Collaboration et al. (2016).

⁵ A second system (Abell 1631) is detected at $z = 0.014$ (Coziol et al., 2009)—see cluster entry in Section 3.1 for details.

resolution increase, though these images are typically used for morphological reference only, unless otherwise noted. Fig. 27(i)–(ix) in Appendix D highlight the ‘dirty flux’ bias introduced due to the snapshot stacking method used which is corrected as described in Section 2.1.2 of Duchesne et al. (2021c). Final imaging details are collected in Table 2. Note FIELD5 was published in Duchesne et al. (2020) and no further sources have been detected in that field so is not discussed here. FIELD4 suffered from significant sidelobe contamination from Cygnus A with the 185- and 216-MHz bands rendered unusable and will not be considered until future observations can be made when Cygnus A is not present in the primary beam sidelobe¹³.

¹³Note that Cygnus A appeared with an apparent flux of $\sim 800 \text{ Jy beam}^{-1}$ at 185 MHz on the horizon for these observations so proved particularly resistant to subtraction/peeling techniques. While images were eventually made, residual errors remain which made the images unusable for this work.

2.3. ASKAP survey data

2.3.1. Data and re-processing

The Rapid ASKAP Continuum Survey (McConnell et al., 2020) at 887 MHz covers the entire sky below $\delta_{J2000} \sim +30^\circ$ and covers all clusters in our sample. The survey has a resolution of ~ 15 arcsec and noise of $\sim 250\text{--}400 \mu\text{Jy beam}^{-1}$. This imaging is sufficient in most cases to detect discrete source populations within the emission regions in the MWA data. ASKAP data (images and calibrated visibilities) are publicly available through the CSIRO¹⁴ ASKAP Science Data Archive (CASDA; Chapman et al., 2017; Huynh et al., 2020). RACS data products are available under project AS110 (Hotan et al., 2020a).

We are able to obtain slightly higher sensitivity in the RACS images by re-imaging with a robust +0.25 weighting using WSClean which has the added benefit of enhancing any detected diffuse

¹⁴Commonwealth Scientific and Industrial Research Organisation

Table 2 MWA-2 and ASKAP observation and image details. Note due to the large number of separate images produced, there is a large range of values and here we report the minimum and maximum values for each quantity for each field. Exact PSF values used in measurements are provided as part of the online table described in Appendix B.

Field/Name/Project	ν (MHz)	Weighting	τ ^a (min)	PSF ^b (" × ")	min(σ_{rms}) (mJy beam ⁻¹)	θ_{max} (')
MWA-2 ^f						
FIELD1 ^c	88–216	+2.0	68(56)	91 × 65(230 × 160)	2.0(8.3)	90
FIELD2		+2.0	62(88)	94 × 68(222 × 165)	1.4(7.9)	120
		+0.5	60(86)	60 × 60(150 × 148)	0.83(5.4)	90
FIELD3		+2.0	22(66)	100 × 66(248 × 157)	3.0(10.9)	120
		0.0	30(46)	60 × 53(152 × 126)	2.3(7.1)	120
FIELD6		+2.0	24(42)	63 × 51(229 × 145)	2.3(10.3)	90
		0.0	24(42)	63 × 51(145 × 118)	2.4(9.7)	90
FIELD7 ^c		+2.0	64(94)	128 × 67(321 × 161)	4.0(12.2)	120
		0.0	56(86)	67 × 52(162 × 125)	2.3(7.0)	120
FIELD8 ^e		+2.0	64(94)	128 × 67(321 × 161)	3.1(16.1)	120
FIELD9		+2.0	124(198)	96 × 67(235 × 163)	2.0(10.0)	90
		0.0	200(216)	59 × 53(140 × 126)	1.2(6.1)	120
FIELD10 ^c		+2.0	64(94)	103 × 67(254 × 161)	2.6(9.9)	120
FIELD11		+1.0	36(38)	79 × 61(194 × 148)	1.5(9.6)	90
ASKAP ^g						
RACS	887	+0.25	15	14.5 × 14.5(22 × 22)	0.12(0.18)	10
		0.0	15	12 × 12(16 × 16)	0.16	10
		+0.25, tapered	15	39 × 39(90 × 90)	0.31(0.60)	10
VAST	887	+0.25	60	16 × 16	0.10	20
		0.0	60	13 × 13	0.075	20
		+0.5, taper	60	50 × 50	0.16	20
SB25035	887	+0.25	780	21 × 21	0.25	20
		+0.25, taper	780	60 × 60	0.70	20
SB15191	943	+0.25	595	12.8 × 12.8	0.026	20

^a Range of total stacked times for MWA snapshots, though note that effective sensitivity varies over the map due to mixed primary beam pointings/patterns. For ASKAP observations, this is simply integration time.

^b Range of major and minor axes of the PSF at the centre of the stacked images for the various images/frequencies.

^c Alternate imaging published in Duchesne et al. (2021c).

^d FIELD7 and FIELD10 have significant enough overlap that they are combined for a joint FIELD7+FIELD10 for increased sensitivity, though two individual maps are made centered on each field.

^e Alternate imaging for this field published in Brüggén et al. (2021) and Duchesne et al. (2021c).

^f For MWA-2 observations, all fields are observed at 88, 118, 154, 185, and 216 MHz, and in general resolution increases with frequency, sensitivity peaks at 154 MHz except for zenith fields where sensitivity peaks at 216 MHz, and integration time varies across frequencies due to difference in data lost to ionospheric problems or other calibration problems. As discussed in the text, FIELD4 and FIELD5 are not presented in this work.

^g All ASKAP data are re-imaged.

emission with only a minor loss in resolution. For clusters where discrete sources are strong enough to be subtracted using a suitable u, v cut (ranging from $1700\text{--}3000\lambda$, additionally see Knowles et al. 2021 for some discussion of this problem), we subtract discrete sources and re-image with additional tapering—dependent on the scale of the emission—at a robust +0.25 image weighting. For a selection of observations where point sources are either too faint or non-existent, a low-resolution image is made without additional subtraction and intervening source contributions (if any) are subtracted from the flux density measurements. As a quick quality assurance check, we compare any re-processed maps to the RACS

survey images and find no significant discrepancies in astrometry or flux scale.

Two clusters in our sample also benefit from being within archival ASKAP observations performed for the ASKAP survey for Variability And Slow Transients (VAST; Murphy et al., 2013) under pilot project AS107 (Murphy et al., 2020). The set up for these observations is similar to RACS, except they have 5–6 ~ 15 min identical pointings which we combine and image as above. These data have some overlap in u, v coverage, so the additional u, v coverage is typically only equivalent to 2–3 additional 15-min observations. Source-subtraction is done in the combined visibilities

and flux densities of point sources are equivalent to within a few per cent of RACS data at the location of the VAST observations.

Abell 0122 features at the centre of a beam in a deep observation, SB25035 (Murphy et al., 2019)¹⁵. These data are processed identically to images presented of Abell 0141 by Duchesne et al. (2021c) and no flux scale discrepancy is observed. Due to the smaller size of the emission, no low-resolution image is made.

Finally, a single cluster, Abell 3186, is present outside of the full width at half maximum (FWHM) of some beams in a deep, 12-h observation near the Large Magellanic Cloud (SB25035; Hotan et al., 2020b). As the primary beam is not well modelled by a simple 2-d Gaussian ~ 2 deg away from the beam centre, we instead cross-match sources in the image to a catalogue derived from the RACS image in the region, and create a pseudo primary beam correction using `flux_warp` with a linear radial basis function interpolation scheme. This results in flux densities of the surrounding point sources that do not differ by more than ~ 10 per cent from RACS. While the point source sensitivity of this image is comparable to the 15-min RACS image, the inner u, v sampling is denser due to the longer synthesis rotation allowing better recovery of extended emission.

While the deep ASKAP observations have a well-sampled u, v plane, as discussed by McConnell et al. (2020), the short ~ 15 -min observations performed for RACS do not allow significant sampling of the inner u, v plane due to lack of significant Earth-rotation synthesis (see e.g. their Figure 4 for an example of the u, v coverage, and see e.g. Figure 2 from Duchesne et al. 2021a for an example of the u, v coverage for a 10-h ASKAP observation). While in principle structures up to ~ 10 arcmin can be recovered, the lower sensitivity at this large angular scale only allows the brightest large-scale objects to be recovered fully. Generally the sources we will discuss in this work are sufficiently small to not be heavily affected (with some exceptions, noted where appropriate) and measurements typically agree with spectra obtained from MWA-2 data alone.

General ASKAP imaging details are presented in Table 2, and as with the MWA-2 data a range of imaging properties are reported for the various RACS images made. For non-RACS images, we report the exact properties.

2.4. Spectral properties

2.4.1. Intervening source contributions

Due to the low resolution of the MWA (even in its extended configuration) we have to carefully consider contamination from confusing sources. The two main scenarios we consider are case (1) brighter sources blended with the diffuse emission, and/or case (2) faint underlying/intervening sources within the detected MWA emission. Case (1) is simple in the sense that bright sources are easily detected with low resolution surveys such as the NVSS or SUMSS, both with ~ 45 arcsec resolution, or the TIFR¹⁶ GMRT¹⁷

¹⁵Additional observations are also available, however, the sensitivity in the single observation used here is sufficient and sensitivity improves only moderately with the additional observations.

¹⁶Tata Institute for Fundamental Research

¹⁷Giant Metrewave Radio Telescope

Sky Survey (TGSS; Intema et al., 2017) with ~ 25 arcsec resolution. The RACS survey data are suitable for this purpose also, and the MWA-2 and GLEAM data can also be useful in this case.

In case (1), we can generally detect these brighter sources across multiple frequencies and model their spectra to remove their contribution in the MWA images, fitting a normal power law model of the form

$$S_{\nu, \text{discrete}} = S_{0, \text{discrete}} (\nu/\nu_0)^\alpha, \quad (1)$$

for extrapolation to $S_{\nu, \text{discrete}}$ from a measured flux density $S_{0, \text{discrete}}$. For sources with only two measurements we derive a two-point spectral index rearranging Eq. (1). We did not encounter any intervening discrete sources that required more complex spectral energy distribution (SED) modelling. Uncertainty in the initial discrete source measurements and spectral index are propagated to the extrapolated value.

Case (2) typically involves sources that are only detected in RACS or other higher-resolution data due to the relative sensitivities of the various low-resolution surveys. If multiple data sets are available, we model the SED as above to extrapolate discrete source flux densities at MWA frequencies. For sources without spectral coverage, we assume a spectral index. Typically this is assumed to be $\langle \alpha \rangle = -0.7$, though for some sources we note a non-detection in some MWA-2 bands/TGSS imply flatter spectra and modify the assumed spectral index appropriately. We use a range of α to estimate additional uncertainty in the unknown spectral index, via:

$$S_{\nu, \text{discrete}} = S_{0, \text{discrete}} \nu^{\langle \alpha \rangle} \pm \sigma_{S_{\nu, \text{discrete}}} [\text{Jy}], \quad (2)$$

and

$$\sigma_{S_{\nu, \text{discrete}}} = S_{0, \text{discrete}} \|\nu^{\alpha_{\min}} - \nu^{\alpha_{\max}}\| [\text{Jy}], \quad (3)$$

where $\alpha_{\min} = -1.0$ and $\alpha_{\max} = -0.5$, typically, though may be chosen to reflect limits on point source contributions as seen in TGSS or MWA images. For each source, we report the total confusing flux density contributions that are subtracted, along with associated uncertainty in the online table (see Appendix B for details of the online table).

2.4.2. Flux density measurements

Flux density measurements are predominantly made using the lower-resolution robust +2.0/+1.0 images along with the GLEAM 200-MHz image and select ASKAP images. For certain sources/fields MWA-2 robust 0.0/+0.5 images are used to maximise the signal-to-noise ratio (SNR) for smaller sources. Flux density measurements are performed using in-house code, `fluxtools.py`¹⁸ by integration over a bespoke polygon region enclosing the source at all frequencies. This means the region is large enough to enclose the emission seen in the lowest-resolution images (usually the 88-MHz maps).

As the MWA-2 images are only CLEANed to the noise level in the individual 2-min snapshots, additional consideration is made for the un-deconvolved/‘dirty’ flux density contribution in the final stacked images. As described in Duchesne et al. (2021c), the measurement of flux density may not be consistent before and after

¹⁸<https://gist.github.com/Sunmish/198ef88e1815d9ba66c0f3ef3b18f74c>,

CLEANing, and the measurement process has the added complexity of normalising the residual, ‘dirty’ flux density to the CLEAN flux density. Fig. 27(i)–(ix) in Appendix D show this effect for simulated Gaussian sources of varying size, highlighting the dependence on source size.

Flux density measurements, S_ν , can therefore be described by

$$S_\nu = \begin{cases} S_{\text{CLEAN}} + S_{\text{dirty}}/f - S_{\nu,\text{discrete}}, & \text{for MWA-2} \\ S_{\text{image}} - S_{\nu,\text{discrete}}, & \text{otherwise} \end{cases} \quad (4)$$

where S_{CLEAN} is the contribution from the stacked CLEAN component model, S_{dirty} is contribution from the stacked residual map, f is the model ratio $S_{\text{dirty}}/S_{\text{CLEAN}}$ determined from simulated Gaussian sources, dependent on source size (Fig. 27(i)–(ix)), and S_{discrete} is the contribution from intervening discrete sources. For the non-MWA-2 images, S_{image} is measured directly from the restored images.

The uncertainty on the flux density measurement, σ_{S_ν} , is estimated as the quadrature sum of the various sources of uncertainty following

$$\sigma_{S_\nu} = \left[(\sigma_{\text{scale}} S_\nu)^2 + (\sigma_{\text{discrete}})^2 + N_{\text{beam}} (\sigma_{\text{rms}})^2 + (\sigma_{\text{std},f} S_{\text{dirty}})^2 \right]^{0.5}, \quad (5)$$

where σ_{scale} is the flux scale uncertainty for the image, $\sigma_{\text{std},f}$ is the standard deviation in values of f over all snapshots for a given stacked MWA-2 image, σ_{discrete} is the uncertainty in the subtracted discrete source contribution, and N_{beam} is the number of independent restoring beams that cover the polygon region used for measurement. Typically the σ_{scale} term dominates, as this is ~ 8 – 10 per cent for all MWA and ASKAP images. The $(\sigma_{\text{std},f} S_{\text{dirty}})^2$ term is only included for MWA-2 images.

2.4.3. Spectra and spectral indices

The measured flux densities and uncertainties are used for modelling the integrated spectra within the observed frequency range. For sources with only MWA-2 data, we find a normal power law (as in Eq. 1) describes the data sufficiently well¹⁹ and provides a spectral index for the source. For sources where additional flux density measurements are available, we find a mixture of power law and curved power law models can be used to describe the observed spectra. We use a generic curved power law model of the form (Duffy & Blundell, 2012)

$$S_\nu \propto \nu^\alpha \exp[q(\ln \nu)^2], \quad (6)$$

where q gives an indication of curvature in the spectrum. For each source we provide a fitted power law model or a curved power law model if appropriate, with the combined MWA-2 and supplementary data. An additional power law model is fit solely to the MWA-2 measurements providing a low-frequency spectral index. Model parameters and uncertainties are estimated via non-linear weighted least-squares curve fitting with the Levenberg–Marquardt algorithm and we report 1σ uncertainties.

Table 3 X-ray observation properties.

Cluster name	Obs. ID	Exp. time ^a (ks)
RXC J0137.2–0912	0765001101	14.4
Abell S0112	0653880201	42.3
MCXC J0154.2–5937	0109460201	6.3
Abell 3186	0692931401	22
	0723161201	
Abell S0405	0720250601	8
PSZ1 G287.95–32.98	0762800101	15
Abell 3399	0692933101 ^b	25
Abell 0550	0675470101	17
	0720250101	

^a Exposure time after the cleaning procedures described in Section 2.5.

^b *Chandra* dataset.

2.5. Archival X-ray observations

X-ray datasets used in this work were taken using the XMM-Newton European Photon Imaging Camera (EPIC, Turner et al. 2001 and Strüder et al. 2001) except for the observation of Abell 3399 which was taken using the Advanced CCD Imaging Spectrometer (ACIS, Garmire et al. 2003) on board of the *Chandra* observatory. The details of data reduction can be found in the Appendix A of Bartalucci et al. (2017). We used the same reduction and cleaning procedures but updated versions of the *Chandra* and XMM-Newton analysis software CIAO (Fruscione et al., 2006) ver. 4.11 with CALDB 4.8.5 and SAS (ver. 15.0) with CCF updated up to March 2021, respectively. The useful exposure times after the cleaning procedures and the observations used are reported in Table 3. The datasets were then arranged in data-cubes and corresponding exposure and background maps were calculated as detailed in Bourdin & Mazzotta 2008, Bourdin et al. 2013 and Bogdán et al. 2013. Point sources were detected using the technique described in Bogdán et al. 2013, visually inspected for false positives or missed sources and then removed from the analysis. Exposure-corrected and background subtracted images are produced in the [0.5–2.5] keV band.

2.6. Additional survey data

In addition to the already discussed radio survey images (NVSS, TGSS, SUMSS, and GLEAM), we make use of images from the ROSAT²⁰ All Sky Survey (RASS; Voges et al., 1999) for select clusters without deep *Chandra* or XMM-Newton observations and optical data from the SuperCOSMOS Sky Survey (SSS; Hambly et al., 2001a,b,c), the first Pan-STARRS²¹ survey (PS1; Tonry et al., 2012; Chambers et al., 2016), and the Dark Energy Survey Data Release 2 (DES DR2; Abbott et al., 2018; Morganson et al., 2018; Flaugher et al., 2015, hereafter DES).

²⁰Röntgen SATellite

²¹Panoramic Survey Telescope And Rapid Response System

¹⁹Though note in low-SNR cases curvature could be hidden in the noise.

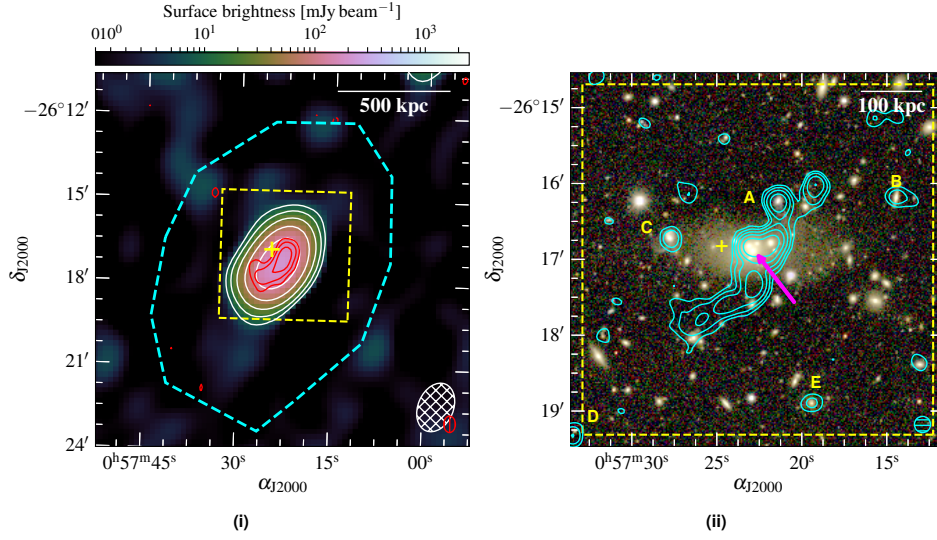


Figure 2. Abell 0122. (i). Background: MWA-2, 185 MHz, robust +2.0 image. (ii). Background: RGB DES image (i , r , g). Where relevant, the white contours are from the background image in (i), in levels of $[\pm 3, 6, 12, 24, 48] \times \sigma_{\text{rms}}$ ($\sigma_{\text{rms}} = 2.5$ mJy beam $^{-1}$). Red contours: TGSS image, in levels of $[\pm 3, 6, 12, 24, 48] \times \sigma_{\text{rms}}$ ($\sigma_{\text{rms}} = 4.5$ mJy beam $^{-1}$). Cyan contours: deep ASKAP robust +0.25 image, in levels of $[\pm 3, 6, 12, 24, 48] \times \sigma_{\text{rms}}$ ($\sigma_{\text{rms}} = 0.026$ mJy beam $^{-1}$). The dashed, yellow box is identical in both panels. The ellipses in the lower corners correspond to the respective beams. Sources discussed in the text are labelled. Linear scale bars are at the redshift of the cluster. The magenta arrow points towards the brightest cluster galaxy (BCG). The yellow cross indicates the reported cluster centre, and the dashed cyan polygon indicates the region used for flux density measurement.

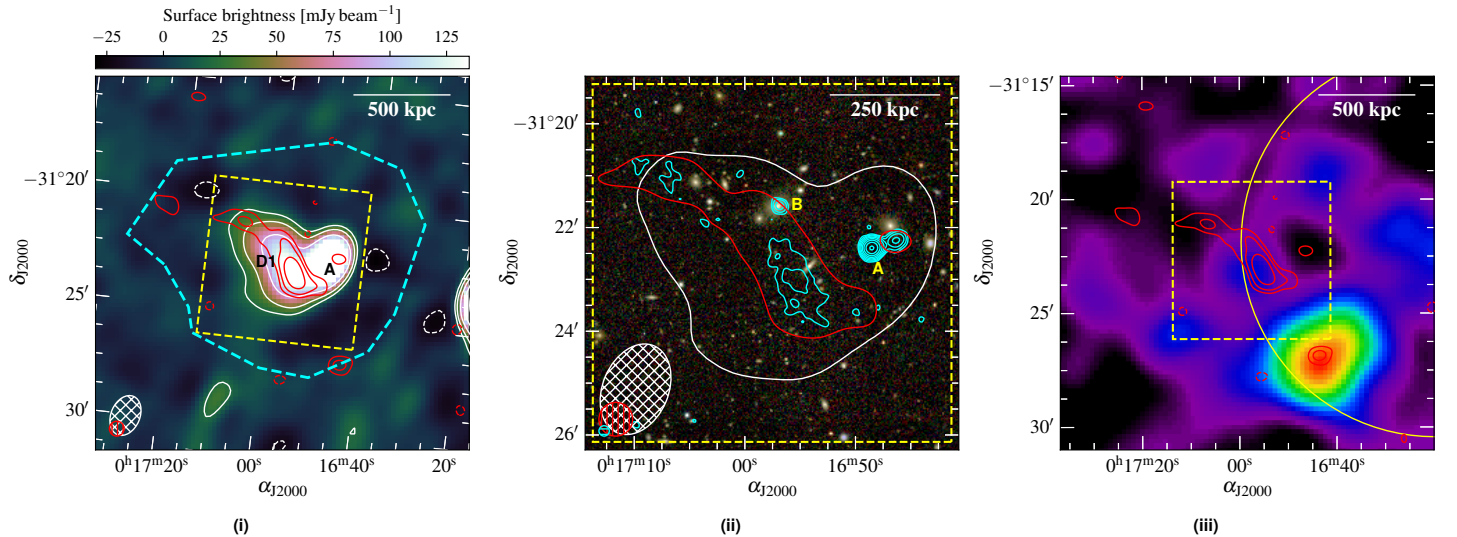


Figure 3. Abell 2751. (i). Background: MWA-2, 185 MHz, robust +2.0 image. (ii). Background: RGB DES image (i , r , g). (iii). Background: Smoothed RASS image. The white contours are as in Fig. 2(i) for the background of (i) ($\sigma_{\text{rms}} = 7$ mJy beam $^{-1}$), except in (ii) with a single contour at $3\sigma_{\text{rms}}$. Red contours: RACS discrete source-subtracted image, $[\pm 3, 6, 12, 24, 48] \times \sigma_{\text{rms}}$ ($\sigma_{\text{rms}} = 0.44$ mJy beam $^{-1}$), except in (ii) with a single contour at $3\sigma_{\text{rms}}$. Cyan contours: RACS robust +0.25 image, $[\pm 3, 6, 12, 24, 48] \times \sigma_{\text{rms}}$ ($\sigma_{\text{rms}} = 0.2$ mJy beam $^{-1}$). The yellow circle in (iii) has a 1 Mpc radius centered on the reported cluster coordinates. Other features are as in Fig. 2.

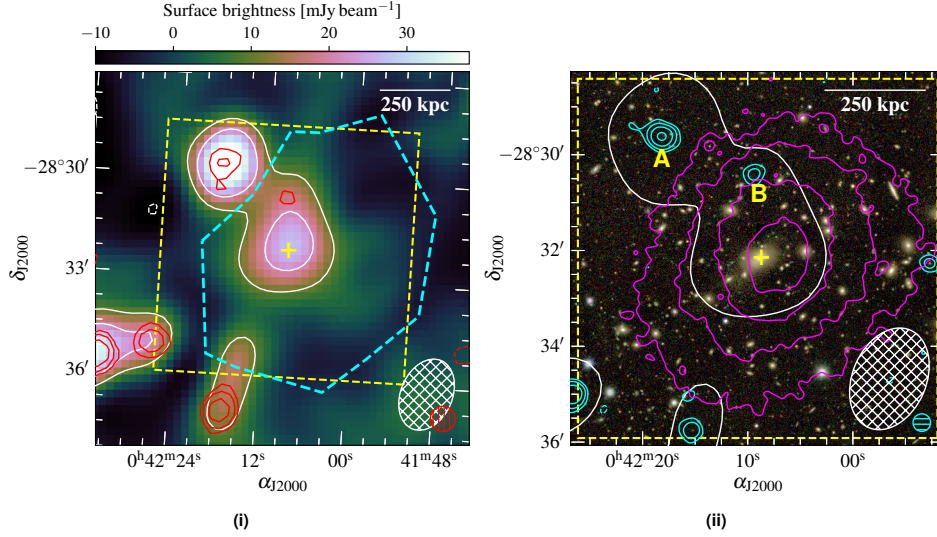


Figure 4. Abell 2811. (i). Background: MWA-2, 154 MHz, robust +2.0 image. (ii). Background: RGB DES image (*i*, *r*, *g*). The white contours are as in Fig. 2(i) for the background of (i) (for $\sigma_{\text{rms}} = 3.5 \text{ mJy beam}^{-1}$). Red contours: NVSS image, in levels of $[\pm 3, 6, 12, 24, 48] \times \sigma_{\text{rms}}$ ($\sigma_{\text{rms}} = 0.45 \text{ mJy beam}^{-1}$). Cyan contours: RACS robust +0.25 image, in levels of $[\pm 3, 6, 12, 24, 48] \times \sigma_{\text{rms}}$ ($\sigma_{\text{rms}} = 0.17 \text{ mJy beam}^{-1}$). Magenta contours: exposure-corrected, background-subtracted XMM-Newton data as presented in D21. Other image features are as in Fig. 2.

3. Results

3.1. Individual clusters

In this section we will describe the individual clusters ordered by observed field. Individual plots of source SEDs are shown in Appendix C and measurements for cluster sources are provided as an online table described in Appendix B.

3.1.1. FIELD1

Abell 0122. (Fig. 2). Reported by D21 as an unclassified steep spectrum source. The source is detected in the MWA-2, TGSS, and deep ASKAP data, shown in Fig. 2(i) and Fig. 2(ii). The deep ASKAP data show a complex source with additional point source contributions (labelled in Fig. 2(ii)) and with contribution from what may be the core of the emission, the brightest cluster galaxy (BCG) (6dF J0057228–261653; Jones et al. 2009) indicated by a magenta arrow in Fig. 2(ii). The projected extent of the source is ~ 2.6 arcmin (corresponding to ~ 310 kpc), including the protrusion to the West of Source A. This is slightly smaller than that reported by D21 due to less source blending. The SED between 88–943 MHz is shown in Fig. 26(i), finding curvature between the MWA and ASKAP data after subtraction of the labelled sources, and with a spectral index from 88–216 MHz of $\alpha_{88}^{216} = -1.6 \pm 0.1$. We consider this a remnant radio galaxy, likely associated with the BCG, or otherwise fossil plasma originally from the BCG.

Abell 2751. (Fig. 3). D21 report a relic source on the outskirts of Abell 2751 (D1 in Fig. 3(i)). We show the MWA-2 and RACS discrete source-subtracted images in Fig. 3(i), and the higher-resolution RACS image in Fig. 3(ii) showing the embedded compact source labelled B. The largest angular size (LAS) is 4.7 arcmin corresponding to a largest linear size (LLS) of 580 kpc, slightly smaller than that reported by D21 due to the less confused images. Sources A and B are subtracted from MWA-2 measurements, and we subtract the contribution of B from the measurements presented in D21. A plot of the SED between 88–1400 MHz is shown in Fig. 26(ii) in Appendix C, and we find a well-fit power law distribution with $\alpha_{88}^{1400} = -1.23 \pm 0.06$, consistent with α reported

by D21. RASS data shown in the Fig. 3(iii) indicates the bulk ICM sits to the southwest, with D1 oriented almost perpendicular, which is abnormal for large-scale relics (with the exception of the relic source in MACS J1149.5+2223, though the nature of that source is unclear; Bonafede et al. 2012; Bruno et al. 2021). With no evidence of shocks (and an absence of more sensitive X-ray data) we cannot differentiate from relic or fossil electrons/remnant radio galaxy. The reported cluster centre by Abell et al. (1989) is offset from the RASS X-ray peak by ~ 2 arcmin (~ 230 kpc); the optical concentration of galaxies is also elongated (Duchesne et al., 2021b, see their Figure 15)—we suggest the system is merging based on these observations, and significant shocks may be present in the cluster volume. We consider this an ambiguous fossil source or remnant.

Abell 2811. (Fig. 4). Halo/mini-halo candidate reported by D21, detected in MWA-2 data up to 185 MHz, with only partial detection at 216 MHz, and no detection in the RACS data (Fig. 4). We measure the integrated flux density across the MWA-2 band, including the 200-MHz GLEAM image, and fit a power law model to the SED (Fig. 26(iii)), finding $\alpha_{88}^{200} = -2.5 \pm 0.4$ ($\alpha_{\text{MWA-2}} = -3.1 \pm 0.5$ for the MWA-2 data only), after subtraction of the contribution of Source B. The 168-MHz measurement reported by D21 is slightly higher than expected due to additional blending with Source A. Additionally, the LAS is 2.7 arcmin (with an LLS of 320 kpc), slightly smaller again due to less blending with Source A. We fit the exposure-corrected and background-subtracted XMM-Newton data presented in D21 with a single- β model (Cavaliere & Fusco-Femiano, 1976), and estimate the X-ray morphological parameters, the centroid shift, w (Poole et al., 2006), with an outer radius set to $R_{500} = 1.035 \text{ Mpc}$ (Piffaretti et al., 2011). We find $w = 0.072 R_{500}$, consistent with disturbed systems (Pratt et al., 2009). Additionally, the surface brightness concentration, $c_{100/500}$ is found to be 0.21, placing it right on the border of merging, halo-hosting clusters (Cassano et al., 2010). Similarly, the centroid shift within 500 kpc is found to be $w_{500} = 0.07$, placing it outside of halo-hosting quadrant, near Abell 697 which has been reported to host a radio halo (but see also Kempner & Sarazin 2001 Venturi et al., 2008)

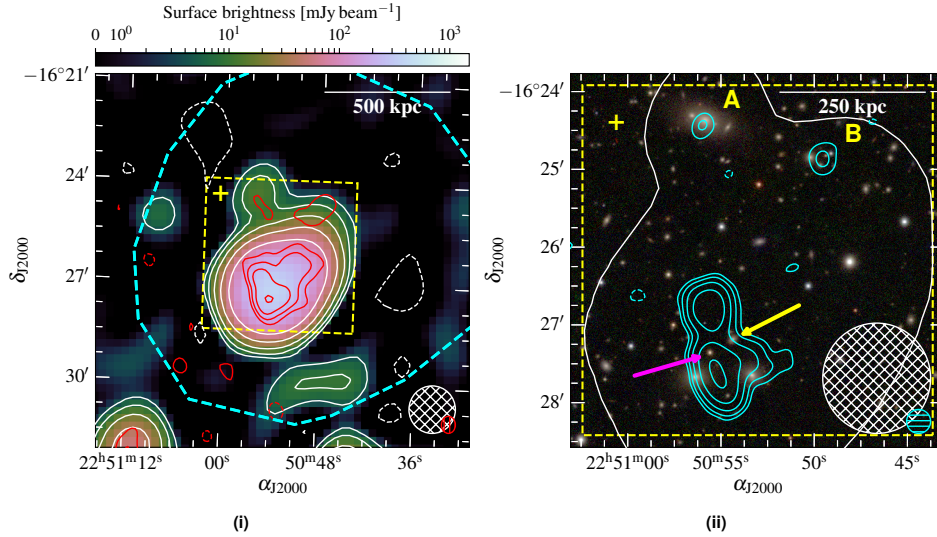


Figure 5. **Abell 2496.** (i). Background: MWA-2, 185 MHz, robust +0.5 image. (ii). Background: RGB PS1 image (*i*, *r*, *g*). The white contours are as in Fig. 2(i) for the background of (i) (for $\sigma_{\text{rms}} = 1.5 \text{ mJy beam}^{-1}$). Red contours: TGSS image, in levels of $[\pm 3, 6, 12, 24, 48] \times \sigma_{\text{rms}}$ ($\sigma_{\text{rms}} = 4 \text{ mJy beam}^{-1}$). Cyan contours: RACS robust +0.25 image, in levels of $[\pm 3, 6, 12, 24, 48] \times \sigma_{\text{rms}}$ ($\sigma_{\text{rms}} = 0.23 \text{ mJy beam}^{-1}$). Other image features are as in Fig. 2.

with an ultra-steep spectrum ($\alpha = -1.5$; Macario et al., 2013), though not as steep as the spectrum for Abell 2811. We also note the concentration parameter, $c_{40/400} = 0.048$, is below what is typically seen in cool-core clusters (CC; Santos et al. 2008, with $c_{40/400} \gtrsim 0.075$). Many of the properties are consistent with a radio halo, however, such a steep spectrum is rare for radio halos: while we consider this an extreme case of an ultra-steep-spectrum radio halo (USSRH) it may be a fossil plasma source projected onto the cluster centre.

3.1.2. FIELD2

Abell 2496. (Fig. 5). Reported by D21 as an unclassified diffuse cluster source. The MWA-2 and TGSS data in Fig. 5(i) show an extended source, with the RACS data in Fig. 5(ii) showing a clear double-lobed morphology. A small extension is seen in the RACS data in the direction of the larger extension seen in the TGSS and MWA-2 images, tracing an older plasma component. The angular and linear extend of the source is the same as reported in D21. The overall emission is modelled with a normal power law with $\alpha_{88}^{1400} = -1.23 \pm 0.05$ (Fig. 26(i)). The PS1 data show possible hosts between the lobes: WISEA J225055.58–162721.0; indicated by a yellow arrow in Fig. 5(ii), and WISEA J225054.36–162710.7; indicated by a magenta arrow, neither with known redshifts. No distinct radio core is seen. We suggest this is a remnant radio galaxy.

Abell 2680. (Fig. 6). Reported by D21. Fig. 6(i) shows the MWA-2 and TGSS radio data, and Fig. 6(ii) the PS1 data with MWA-2 and RACS data overlaid. The LAS of the source is 3.0 arcmin (with an LLS of 580 kpc), slightly larger than reported by D21 and the reduced confusion enables a better estimate of the size. A single compact source is detected within the emission with RACS (Source A) and is subtracted from subsequent flux density measurements. We are only able to provide measurements in the 88-, 118-, and 154-MHz MWA-2 bands as the cluster is towards the edge of FIELD2 with lessened sensitivity in the higher frequency images. We find $\alpha_{88}^{200} = -1.7 \pm 0.7$ (Fig. 26(v)), consistent with the limited reported by D21. Smoothed RASS data is shown in Fig. 6(iii) highlighting the location of the radio emission relative to

the thermal ICM though noting that the RASS data provide limited insight to the morphology of the ICM. From an optical analysis, Wen & Han (2015, but see also Wen et al. 2012) report an R_{500}^{22} of 1.26 Mpc which corresponds to mass of $M_{500} = 2.4 \times 10^{14} M_{\odot}$ following Equation 1 from Wen & Han (2015). As the cluster is detected in the RASS data, a mass is estimated following the procedures described by Tarrío et al. (2016, 2018), resulting in $M_{500} = 3.2^{+0.8}_{-1.0} \times 10^{14} M_{\odot}$, somewhat consistent with the mass derived from the optical radius. We consider this a candidate halo. **Abell 2693.** (Fig. 7). Reported by D21. The candidate radio halo in Abell 2693 is largely similar to that in Abell 2680, with only a faint discrete source detected in the RACS data (Source A) with $S_{A,887} \sim 0.8 \text{ mJy}$. We provide additional flux density measurements, subtracting the contribution of Source A, to obtain a spectral index of $\alpha_{88}^{200} = -1.5 \pm 0.2$ (Fig. 26(vi)). A mass is derived from the RASS data: $M_{500} = 2.1^{+0.5}_{-0.6} \times 10^{14} M_{\odot}$, placing Abell 2693 as one of the least massive halo-hosting clusters if confirmed (surpassed only by the ‘Ant’ cluster; Botteon et al., 2021b). The LAS for the source is 2.0 arcmin (LLS = 370 kpc), marginally smaller than that reported by D21. Alternatively, this may be a point source with $\alpha_{88}^{887} = -2.2 \pm 0.2$.

Abell S1099. (Fig. 8). Reported by D21. MWA-2 radio data shown in Fig. 8(i) and PS1 optical data shown in Fig. 8(ii). RACS data shows no additional discrete sources beyond Source A, which is subtracted from flux density measurements where appropriate with $\alpha_{A,216}^{1400} = -0.5 \pm 0.1$. The resulting spectral index of the diffuse source D1 is found to be $\alpha_{88}^{1400} = -0.87 \pm 0.11$ (Fig. 26(vii)). The lack of obvious core or any clear lobes/hot spots suggests a remnant radio source that has diffused into the surrounding medium. No deep X-ray observations are available, no cluster or source is detected in the RASS image, and there is no detection as a *Planck*-SZ source. We consider this a remnant radio galaxy with the putative host (LEDA 195207) indicated by a magenta arrow on Fig. 8(ii).

AqrCC 087. (Fig. 9). The cluster is reported in the Aquarius cluster catalogue (Caretta et al., 2002), though no redshift is available.

²²Radius within which the mean density of the cluster is 500 times the critical density of the Universe.

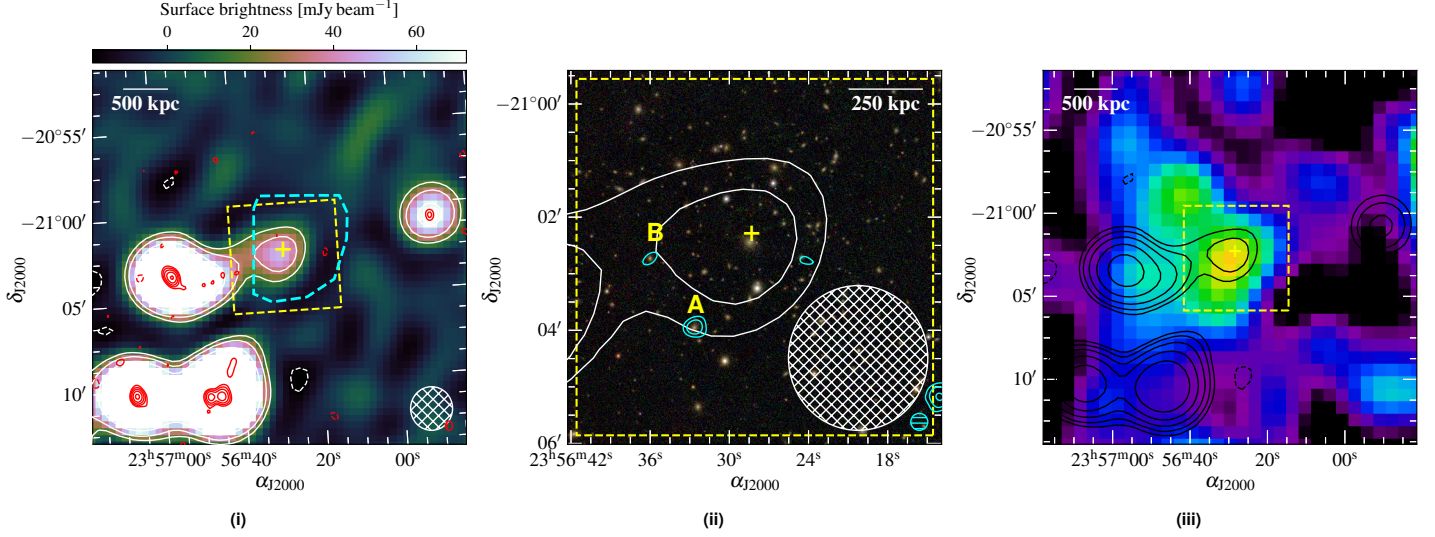


Figure 6. *Abell 2680.* (i). Background: MWA-2, 88 MHz, robust +0.5 image. (ii). Background: RGB PS1 image (*i*, *r*, *g*). (iii). Background: Smoothed RASS image. The white (black) contours are as in Fig. 2(i) for the background of (i) (with $\sigma_{\text{rms}} = 5.5 \text{ mJy beam}^{-1}$). Red contours: TGSS image, in levels of $[\pm 3, 6, 12, 24, 48] \times \sigma_{\text{rms}}$ ($\sigma_{\text{rms}} = 3.7 \text{ mJy beam}^{-1}$). Cyan contours: RACS robust +0.25 image, in levels of $[\pm 3, 6, 12, 24, 48] \times \sigma_{\text{rms}}$ ($\sigma_{\text{rms}} = 0.25 \text{ mJy beam}^{-1}$). Other image features are as in Fig. 2.

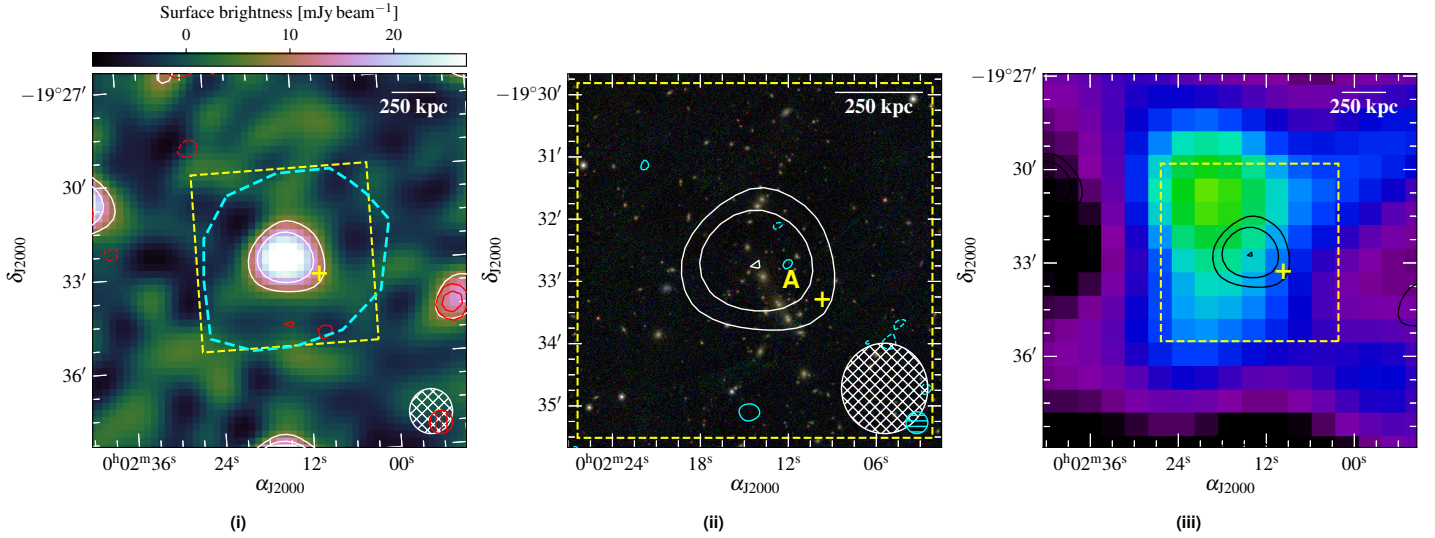


Figure 7. *Abell 2693.* (i) Background: MWA-2, 154 MHz, robust +0.5 image. (ii). Background: RGB PS1 image (*i*, *r*, *g*). (iii). Background: Smoothed RASS image. The white (black) contours are as in Fig. 2(i) for the background of (i) (with $\sigma_{\text{rms}} = 2.8 \text{ mJy beam}^{-1}$). Red contours: NVSS image as in Fig. 4(i). Cyan contours: RACS robust +0.25 image, in levels of $[\pm 3, 6, 12, 24, 48] \times \sigma_{\text{rms}}$ ($\sigma_{\text{rms}} = 0.15 \text{ mJy beam}^{-1}$). Other image features are as in Fig. 2.

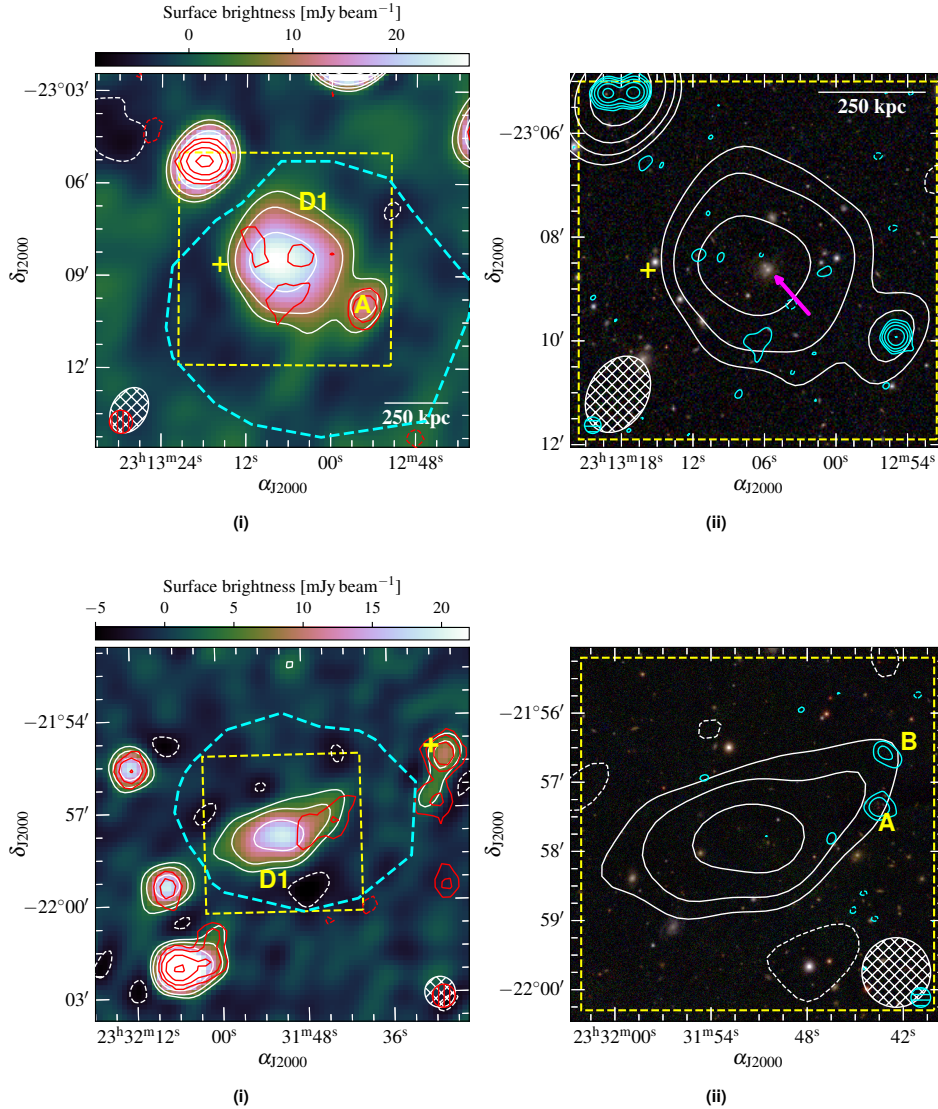


Figure 8. *Abell S1099.* (i) Background: MWA-2, 216-MHz, robust +2.0 image. (ii) Background: RGB PS1 image (*i*, *r*, *g*). The white contours are as in Fig. 2(i) for the background of (i) (with $\sigma_{\text{rms}} = 1.6 \text{ mJy beam}^{-1}$). Red contours: NVSS image as in Fig. 4(i). Cyan contours: RACS robust +0.25 image, in levels of $[\pm 3, 6, 12, 24, 48] \times \sigma_{\text{rms}}$ ($\sigma_{\text{rms}} = 0.19 \text{ mJy beam}^{-1}$). Other image features are as in Fig. 2.

Figure 9. *AqrCC 087.* (i) Background: MWA-2, 216-MHz, robust +0.5 image. (ii) Background: RGB PS1 image (*i*, *r*, *g*). The white contours are as in Fig. 2(i) for the background of (i) (with $\sigma_{\text{rms}} = 1.1 \text{ mJy beam}^{-1}$). Red contours: NVSS image as in Fig. 4(i). Cyan contours: RACS robust +0.25 image, in levels of $[\pm 3, 6, 12, 24, 48] \times \sigma_{\text{rms}}$ ($\sigma_{\text{rms}} = 0.15 \text{ mJy beam}^{-1}$). Other image features are as in Fig. 2, though note no scalebar is given as no redshift is available for the reported cluster.

Additionally, there is no cross-identification with other cluster catalogues, and as with Abell S1099 no X-ray or SZ observations provide detections. We suggest this is a poor cluster or group. The redshift distribution of galaxies within 1 deg around AqrCC 087 peaks around $z \approx 0.1$. We detect an elongated radio source ~ 5.6 arcmin from the reported cluster centre (Fig. 9(i), ~ 620 kpc at $z = 0.1$) with no obvious optical host (Fig. 9(ii)). The angular size is ~ 4.5 arcmin, which if at $z = 0.1$ is a linear projected extent of ~ 500 kpc. The source is not detected in RACS, with a partial detection in the NVSS image (though note there is confusion with the discrete Source A). Source A is subtracted from subsequent MWA-2 flux density measurements, and we obtain a spectral index of $\alpha_{88}^{216} = -1.7 \pm 0.1$ (Fig. 26(viii)). As with Abell S1099, we consider this likely to be a remnant radio galaxy.

RXC J2351.0–1954 (PSZ1 G057.09–74.45). (Fig. 10). Originally D21 reported three candidate sources: a halo at the centre (labelled D1 in Fig. 10(i)), and two relics: SE (labelled D2, inset Fig. 10(iii)), and NW, (labelled D3, inset Fig. 10(ii)). The candidate halo is shown by the RACS data to be blended sources. The SE candidate

relic detected at low significance ($\sim 3\sigma$), though the RACS data show a single compact source within the southern portion of the emission (Source A). The NW candidate relic is partially detected in RACS, with other compact blended sources (B–D in Fig. 10(ii)). Excluding point sources, the LAS of D2 and D3 are 1.9 arcmin (LLS = 230) and 3.5 arcmin (LLS = 430 kpc), respectively. All labelled compact sources are subtracted from MWA measurements where appropriate. The spectral index of D2 is measured to be $\alpha_{\text{D2},88}^{216} = -1.3 \pm 0.3$ (Fig. 26(ix)). D3 shows significant curvature within the MWA band and to 887.5 MHz and is fit with a generic curved model, with a power law model fit across the MWA-2 band: $\alpha_{\text{D3},88}^{216} = -1.2 \pm 0.1$ (Fig. 26(x)). The smoothed RACS image is shown as contours on Fig. 10(i) showing elongation hinting at an un-relaxed ICM, though we consider that D3 is likely a remnant with the classical spectral steepening and D2 is still unconfirmed.

3.1.3. FIELD3

Abell 0168. Fig. 11 shows the radio relic that was reported by Dwarakanath et al. (2018) and is detected in the MWA-2 data.

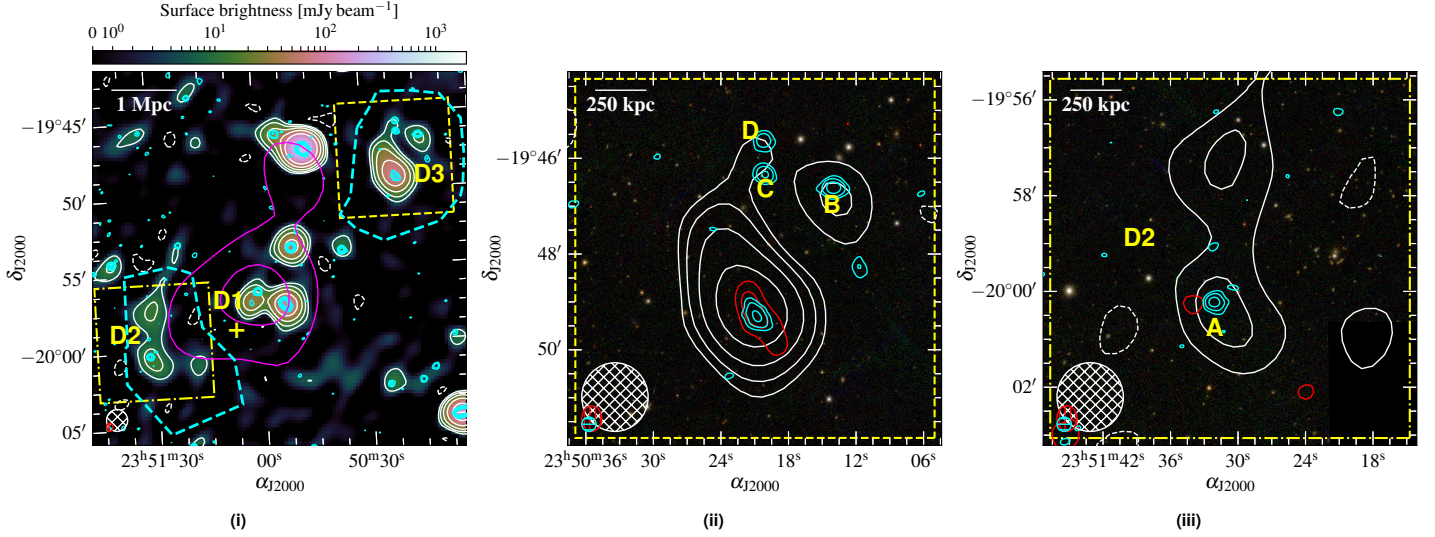


Figure 10. *RXC J2351.0–1954.* (i) Background: MWA-2, 154-MHz, robust +0.5 image. (ii) and (iii) Background: RGB PS1 image (*i, r, g*). The white contours are as in Fig. 2(i) for the background of (i) (with $\sigma_{\text{rms}} = 4.9 \text{ mJy beam}^{-1}$). Red contours: TGSS image, in levels of $[\pm 3, 6, 12, 24, 48] \times \sigma_{\text{rms}}$ ($\sigma_{\text{rms}} = 3.6 \text{ mJy beam}^{-1}$). Cyan contours: RACS robust +0.25 image, in levels of $[3, 6, 12, 24, 48] \times \sigma_{\text{rms}}$ ($\sigma_{\text{rms}} = 0.20 \text{ mJy beam}^{-1}$). Magenta contours: smoothed RASS image, increasing with factors of $\sqrt{2}$. Other image features are as in Fig. 2.

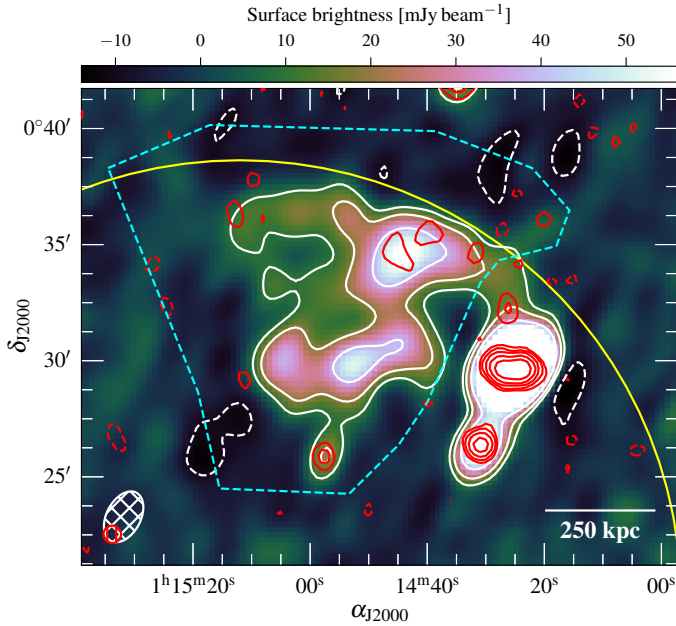


Figure 11. *Abell 0168.* Background: MWA-2, 154-MHz, robust +2.0 image. The white contours are as in Fig. 2(i) for the background image (with $\sigma_{\text{rms}} = 3.2 \text{ mJy beam}^{-1}$). Red contours: NVSS, $[\pm 3, 6, 12, 24, 48] \times \sigma_{\text{rms}}$ ($\sigma_{\text{rms}} = 0.45 \text{ mJy beam}^{-1}$). Other image features are as in Fig. 2, with a yellow circle with a 1 Mpc radius centered on the cluster.

Dwarakanath et al. (2018) split the total relic source into two distinct components—a large exterior component and a smaller interior component with a steeper spectrum. Here we consider it a single emission region due in part to the limitation of resolution but there also appears to be a fainter diffuse component connecting the two regions. While emission is detected in all MWA-2 bands

(see e.g. 118-MHz in Fig. 11), due to the large size (~ 11.5 arcmin) we note that flux recovery diminishes significantly in the 154-, 185-, and 216-MHz bands. With supplemental GLEAM data and flux densities reported by Dwarakanath et al. (2018), we find the spectral index of the whole relic to be $\alpha_{88}^{608} = -1.50 \pm 0.08$.

RXC J0137.2–0912. (Fig. 12). We report the detection of steep-spectrum emission within RXC J0137.2–0912, shown in Fig. 12(i) in MWA and TGSS data. Fig. 12(ii) shows the optical host of the central compact emission with contours from re-processed VAST data (cyan) overlaid. Fig. 12(iii) shows the extent of the cluster’s X-ray emission with archival XMM-Newton data, noting some elongation perpendicular to the orientation of the radio emission. The compact emission from Sources A and B is subtracted after extrapolating to MWA-2 frequencies using the VAST and TGSS measurements, and C–E are subtracted assuming $\alpha = -0.7$. A power law SED is modelled, with a spectral index of $\alpha_{88}^{887} = -1.62 \pm 0.07$ (Fig. 26(xii)), or $\alpha_{88}^{216} = -1.5 \pm 0.1$ across the MWA band alone). The total angular size of the source is 7.8 arcmin, corresponding to 410 kpc. From the archival XMM-Newton data, we find a concentration parameter $c_{40/400} = 0.19$, consistent with cool-core (CC) clusters (where non-CC clusters are found to have $c_{40/400} \lesssim 0.075$; Santos et al. 2008). Based on the likelihood of a CC, the prominent BCG with significant AGN emission, and steep-spectrum diffuse emission surrounding the BCG we suggest the emission is a mini-halo. Some structure in the centre of the cluster gives some evidence for sloshing, and with a centroid shift within $R_{500} = 684 \text{ kpc}$ (Piffaretti et al., 2011) of $w = 0.037 R_{500}$ suggesting some disturbance (Pratt et al., 2009; Böhringer et al., 2010). While the orientation of the radio emission appears largely perpendicular to the X-ray emission, the extension to the SW in the radio is traced by an extension in the X-ray as well. The NE direction is ambiguous as the XMM-Newton exposure drops significantly due to a chip gap at that location. This is indicated on Fig. 12(iii)

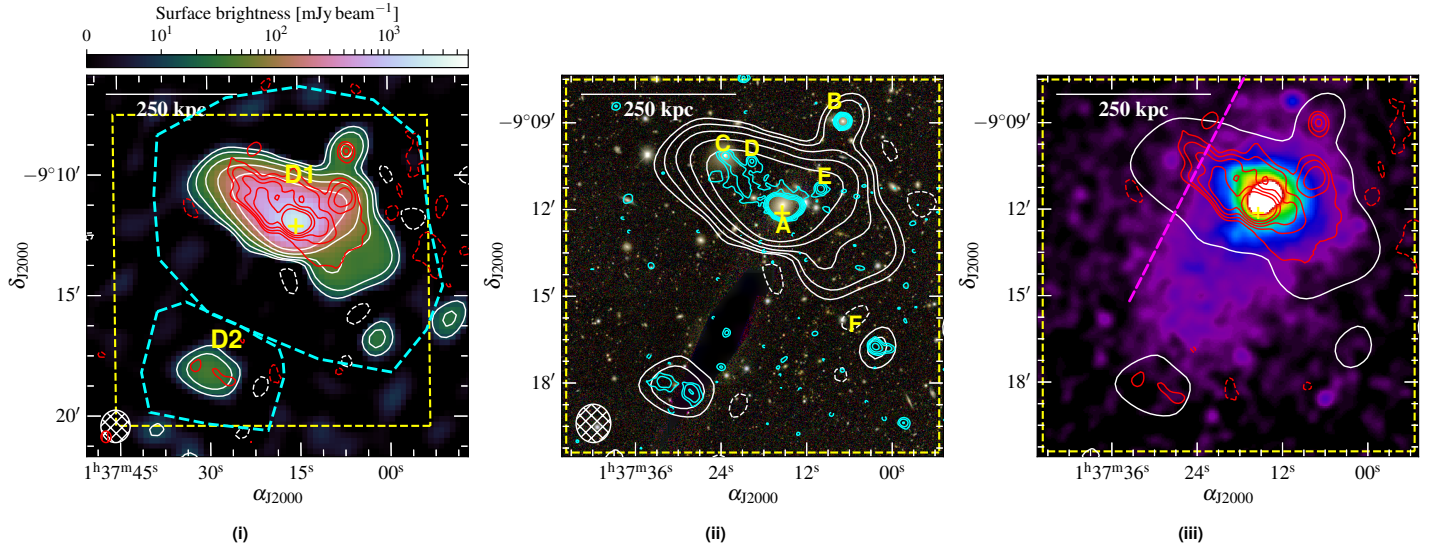


Figure 12. *RXC J0137.2-0912.* (i) Background: MWA-2, 154-MHz, robust 0.0 image. (ii) Background: RGB DES image (*i*, *r*, *g*). (iii). Background: smoothed XMM-Newton EPIC image. The white contours are as in Fig. 2(i) for the background of (i) (with $\sigma_{\text{rms}} = 3.8 \text{ mJy beam}^{-1}$). Red contours: TGSS image, in levels of $[\pm 3, 6, 12, 24, 48] \times \sigma_{\text{rms}}$ ($\sigma_{\text{rms}} = 2.8 \text{ mJy beam}^{-1}$). Cyan contours: VAST +0.25 image, in levels of $[\pm 3, 6, 12, 24, 48] \times \sigma_{\text{rms}}$ ($\sigma_{\text{rms}} = 0.14 \text{ mJy beam}^{-1}$). The dashed, magenta line on (iii) indicates the location of an XMM-Newton chip gap with lessened sensitivity. Other image features are as in Fig. 2.

as a dashed, magenta line.

We see also an additional diffuse source resembling a remnant radio galaxy, D2; however, its SED shows significant curvature uncharacteristic of remnants (Fig. 26(xiii)).

3.1.4. FIELD6

Abell S0112. (Fig. 13). Abell S0112 is covered by the Australia Telescope Low Brightness Survey (ATLBS, region B; Subrahmanyan et al., 2010; Thorat et al., 2013) which reveals two extended radio galaxies (A and B) within the cluster. The MWA data reveal an additional emission component (D1) between the two bright radio galaxies, creating an asymmetric dumbbell shape. The emission is only detected across the MWA-2 band, from 88–185 MHz and in the 200-MHz GLEAM data. The extent of the emission between the two radio galaxies is ~ 3 arcmin (LLS ≈ 230 kpc). We measure integrated flux density within the D1 region between A and B, finding a spectral index of $\alpha_{88}^{185} = -1.9 \pm 0.5$ (Fig. 26(xiv)). In Fig. 13(ii) we show optical data which reveals a lack of obvious optical host for the emission, and Fig. 13(iii) shows the XMM-Newton image, highlighting the offset of the emission from the main component of the X-ray-emitting ICM. Source A is an active radio galaxy with a normal radio spectrum ($\alpha \sim -0.8$), and D1 may be associated with an older episode of outflow. This could be true for B as well, with the extension of B to the north in the MWA-2 data also suggesting additional emission components not detected in higher-frequency/resolution images. We consider this emission fossil plasma associated with either A or B, with potential for some re-acceleration due to the dynamic nature of the cluster.

MCXC J0145.2-6033. (Fig. 14). We report the detection of a candidate mini-halo in MWA-2 and RACS data, shown in Fig. 14(i). The detection is marginal in the RACS data, and 2σ contours of the low resolution image are shown in Fig. 14(i) to highlight the extent of the emission. Fig. 14(ii) shows the robust +0.25 RACS

data which stems from the BCG and extends northwards. We measure the flux densities across the available images and find $\alpha_{88}^{887} = -2.1 \pm 0.1$ (Fig. 26(xv), with the same value across only the MWA-2 band). The extent of the source is LAS = 1.9 arcmin; LLS = 350 kpc. The optical data is shown in Fig. 14(ii), with a BCG clear near the centre of the emission. RACS data shown in Fig. 14(iii) does not show any significant offset from the BCG, and we suggest the cluster is reasonably relaxed. With an LAS of 1.9 arcmin (LLS = 350 kpc), the source is only barely extended in the robust +2.0 MWA-2 images, and the robust 0.0 images show no significant extension. There is a ~ 20 mJy difference between the 0.0 and +2.0 measurements at 154 MHz ($S_{0.0} = 110 \pm 10$ and $S_{2.0} = 130 \pm 10$) which may be allowable within uncertainties. Given the low SNR in the RACS data, it is difficult to confirm if this is an ultra-steep spectrum point source.

MCXC J0154.2-5937. (Fig. 15). We report peripherally located, elongated extended emission in the cluster, shown in Fig. 15(i). In Fig. 15(ii) a potential optical host is seen with matching emission in the RACS image (Source A, $S_{887} \sim 1$ mJy, WISEA J015436.21-593929.9, no redshift). The radio SED of the whole source is uncertain, but consistent with a radio galaxy ($\alpha_{88}^{887} = -0.65 \pm 0.13$; Fig. 26(xvi)). If in the cluster, the source is ~ 1 Mpc in projected extent, classing it as a giant radio galaxy.

3.1.5. FIELD7

Abell 3186. (Fig. 16). From the data presented here we report Abell 3186 to be a double relic system, potentially with central diffuse emission possible from a radio halo. The cluster shows a similar morphology to older observations of the canonical double relic cluster Abell 3667 (Johnston-Hollitt, 2003; Hindson et al., 2014) with a larger, bright relic on one side and a smaller dimmer one on the other.

The larger relic, D1, is detected to the SW as an elongated

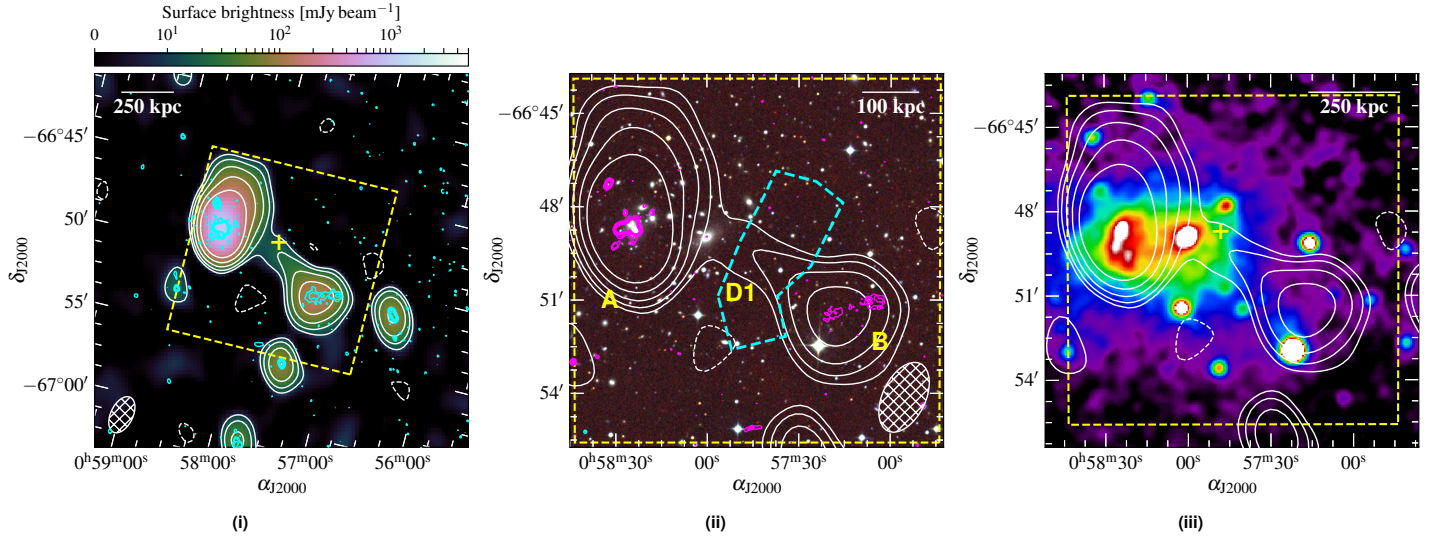


Figure 13. *Abell S0112.* (i) Background: MWA-2, 154-MHz, robust +2.0 image. (ii) Background: RGB SSS image (*i*, *r*, *b*). (iii). Background: smoothed XMM-Newton EPIC image. The white contours are as in Fig. 2(i) for the background of (i) (with $\sigma_{\text{rms}} = 3.5 \text{ mJy beam}^{-1}$). Magenta contours: ATLBS high-resolution image, in levels of $[\pm 3, 6, 12, 24, 48] \times \sigma_{\text{rms}}$ ($\sigma_{\text{rms}} = 0.08 \text{ mJy beam}^{-1}$). Cyan contours: RACS survey image, in levels of $[\pm 3, 6, 12, 24, 48] \times \sigma_{\text{rms}}$ ($\sigma_{\text{rms}} = 0.29 \text{ mJy beam}^{-1}$). Other image features are as in Fig. 2.

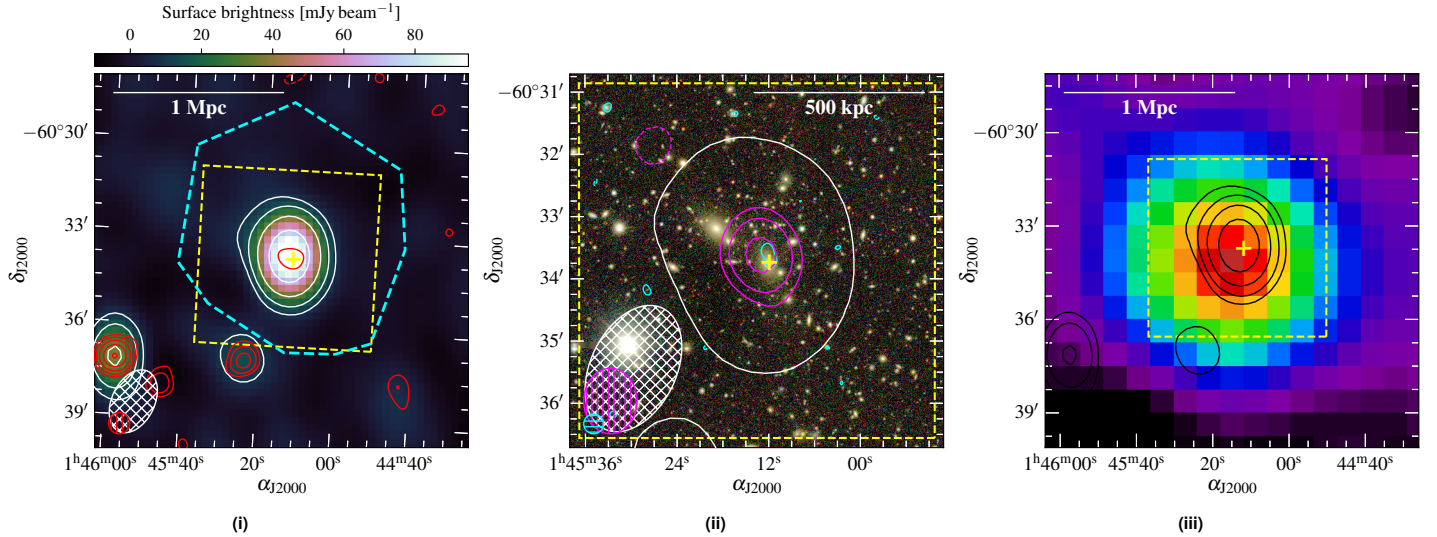


Figure 14. *MCXC J0145.2-6033.* (i) Background: MWA-2, 154-MHz, robust +2.0 image. (ii) Background: RGB DES image (*i*, *r*, *g*). (iii). Background: smoothed RASS image. The white (black) contours are as in Fig. 2(i) for the background of (i) (with $\sigma_{\text{rms}} = 2.9 \text{ mJy beam}^{-1}$). Red contours: RACS low-resolution image, $[\pm 3, 6, 12, 24, 48] \times \sigma_{\text{rms}}$ ($\sigma_{\text{rms}} = 0.34 \text{ mJy beam}^{-1}$). Cyan contours: RACS robust +0.25 image, $[\pm 3, 6, 12, 24, 48] \times \sigma_{\text{rms}}$ ($\sigma_{\text{rms}} = 0.17 \text{ mJy beam}^{-1}$). Magenta contours: MWA-2, 216-MHz, robust 0.0 image, $[\pm 3, 6, 12, 24, 48] \times \sigma_{\text{rms}}$ ($\sigma_{\text{rms}} = 3.4 \text{ mJy beam}^{-1}$). Other image features are as in Fig. 2.

structure on the periphery of Abell 3186 with the MWA and ASKAP, shown in Fig. 16(i). The angular extent of D1 is ~ 12 arcmin, corresponding to ~ 1650 kpc. The MWA-2 images in this region at 154-, 185-, and 216-MHz, which are generally less sensitive, suffered from significant noise from a nearby bright source and the large relic is poorly detected. A somewhat compact source is detected within the emission (Source A) which has a faint, blue optical counterpart, seen in Fig. 16(iii). After subtracting the contribution from A, we obtain a spectral index of $\alpha_{\text{D1},88}^{887} = -1.0 \pm 0.1$ (Fig. 26(xvii)), consistent with relic sources. We show the XMM-Newton image in Fig. 16(ii), and note that Lovisari et al.

(2017) report the cluster has a ‘mixed’ morphology (i.e. semi-disturbed). Additionally, the cluster hosts a second relic to the NW seen as a patchy structure, with detections in all bands, though the full extent of the emission (~ 14 arcmin, ~ 1900 kpc), extending to the SW, is only seen at 88 and 118 MHz as with D1. After subtraction of discrete source contributions (labelled B and C in Fig. 16(iv)), we derive a spectral index of $\alpha_{\text{D2},88}^{887} = -0.9 \pm 0.1$. The morphology and spectral properties of these relics are extremely reminiscent of Abell 3667 which as a bright, larger relic and a smaller more compact relic with average spectral indices of -0.9 for both across MWA bands (Hindson et al., 2014), though higher

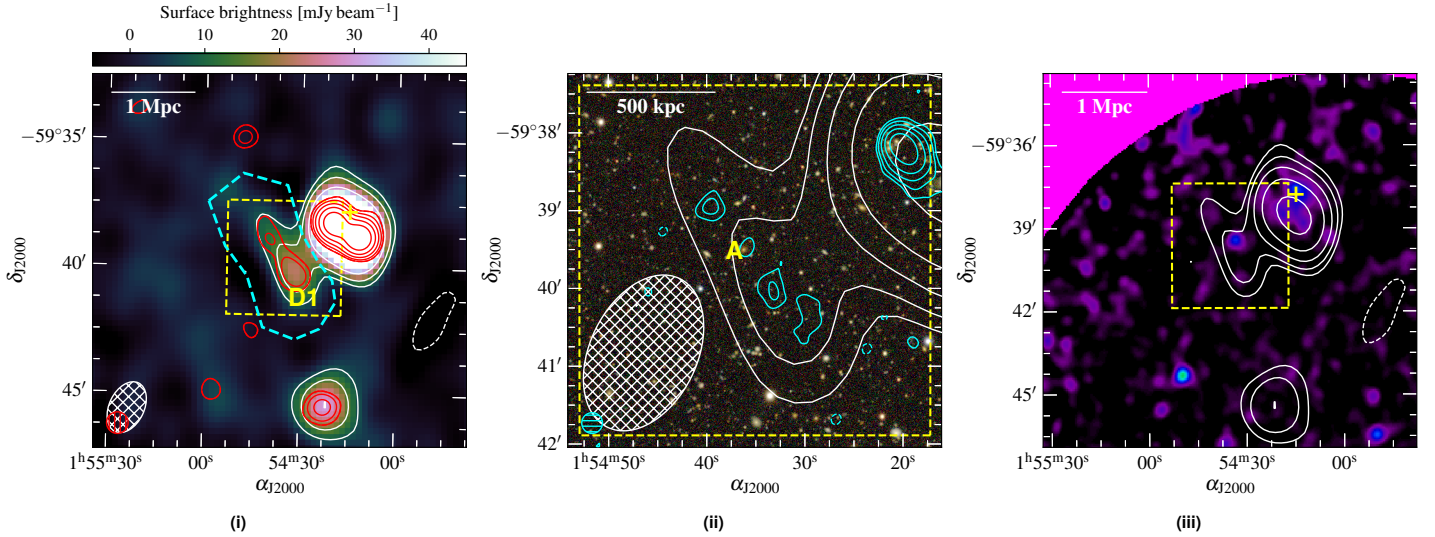


Figure 15. MCXC J0154.2-5937. (i) Background: MWA-2, 154-MHz, robust +2.0 image. (ii) Background: RGB DES image (*i*, *r*, *g*). (iii). Background: smoothed XMM-Newton EPIC image. The white contours are as in Fig. 2(i) for the background of (i) (with $\sigma_{\text{rms}} = 2.5 \text{ mJy beam}^{-1}$). Red contours: RACS low-resolution image, $[\pm 3, 6, 12, 24, 48] \times \sigma_{\text{rms}}$ ($\sigma_{\text{rms}} = 0.40 \text{ mJy beam}^{-1}$). Cyan contours: RACS robust +0.0 image, $[\pm 3, 6, 12, 24, 48] \times \sigma_{\text{rms}}$ ($\sigma_{\text{rms}} = 0.20 \text{ mJy beam}^{-1}$). Other image features are as in Fig. 2.

resolution, higher frequency spectral index measurements show α varies inside the relics from approximately -0.8 to -1 (Johnston-Hollitt, 2003). We consider this a classical double relic system. We note also the 88-MHz MWA-2 image (Fig. 16(i)) appears to show an excess of diffuse flux within the central cluster region which may indicate a radio halo, though the confusion from sources in the cluster make this impossible to confirm with the present data.

Abell S0405. (Fig. 17). We report a diffuse source in Abell S0405, with RACS data revealing a double-lobed radio galaxy structure (Fig. 17(i)) without a core or jets. No obvious optical host exists between the two lobes (Fig. 17(ii)) and we suggest this is a remnant radio galaxy. We find $\alpha_{88}^{887} = -1.99 \pm 0.08$ between the MWA and RACS data, after subtraction of Sources A and B from the MWA images (Fig. 26(xix)). The source is measured to be $\sim 185 \text{ kpc}$ if at the redshift of the cluster ($z = 0.0613$; De Grandi et al. 1999), and sits within the X-ray-emitting ICM (Fig. 17(iii)).

PSZ1 G287.95-32.98.²³ (Fig. 18). We report the detection of a diffuse source at the cluster centre with the MWA at 118 and 154 MHz as well as a partial detection at 887 MHz in RACS data. The projected size of the source is $\sim 320 \text{ kpc}$. Other MWA bands either suffer from lack of sensitivity or significant confusion with nearby Sources A and B (Fig. 18(i)). We obtain a spectral index of $\alpha_{118}^{887} = -1.5 \pm 0.2$ (Fig. 26(xx)). Fig. 18(iii) shows the XMM-Newton image, highlighting the central location of the candidate radio halo. Based on the XMM-Newton data, Rossetti et al. (2017) use the concentration parameter (see Santos et al., 2008) to determine the cluster is a non-CC cluster, and the emission is therefore unlikely to be a mini-halo. Additionally, no obvious BCG with core radio emission is seen in the optical data shown in Fig. 18(ii). We classify this source as a candidate radio halo.

²³Not to be confused with the double-relic system, PLCK G287.0+32.9 reported by Bagchi et al. (2011).

3.1.6. FIELD8

Abell 3399. (Fig. 19). We report the detection of a candidate radio relic on the periphery of Abell 3399 (D1 in Fig. 19(i)) with an angular extent of $\sim 3.6 \text{ arcmin}$ (LLS $\approx 710 \text{ kpc}$) and a candidate radio halo at the centre of the cluster (D2 in Fig. 19(i)) with an angular extent of $\sim 2.8 \text{ arcmin}$ (LLS $\approx 570 \text{ kpc}$). As is clear from the *Chandra* X-ray data shown in Fig. 19(iii), the cluster is undergoing a merger and Lovisari et al. (2017) consider the cluster ‘disturbed’ based on morphological analysis. Measuring flux densities of D1 at 88–154, and 887.5 MHz yields a spectral index of $\alpha_{\text{D1},88}^{887} = -1.6 \pm 0.3$ (Fig. 26(xxi)). For D2, the emission is barely detected between 154–216 MHz and the 88-MHz image is too confused with D1 for a useful measurement. We instead calculate the two-point spectral index between 118 and 887 MHz, finding $\alpha_{\text{D2},118}^{887} = -1.5 \pm 0.2$ (Fig. 26(xxii)), though note the line shown is derived from the two-point index and not a fitted power law model).

3.1.7. FIELD9

MCXC J1253.2-1522 (Abell 1631). (Fig. 20). We report a steep spectrum source projected onto MCXC J1253.2-1522 in MWA data, with no counterpart in RACS, and marginal detection in the TGSS image (Fig. 20(i)). Note the TGSS image has artefacts from the nearby complex radio galaxy that peak at the location of the diffuse source. Multiple cluster systems are reported along line of sight: MCXC J1253.2-1522 at $z = 0.0462$ (Piffaretti et al., 2011) and Abell 1631 at $z = 0.01394$ (Coziol et al., 2009). Additionally, Flin & Krywult (2006) report that the system has complex substructure, which is clear in the smoothed RASS image shown in Fig. 20(iii). No obvious optical host is visible in PS1 data (Fig. 20(ii)), and the projected linear extent is 200 kpc (or 70 kpc if at $z = 0.01394$). While just outside of the field-of-view (FoV) of archival XMM-Newton observations, RASS shows no significant X-ray emission at the location of the source, but the

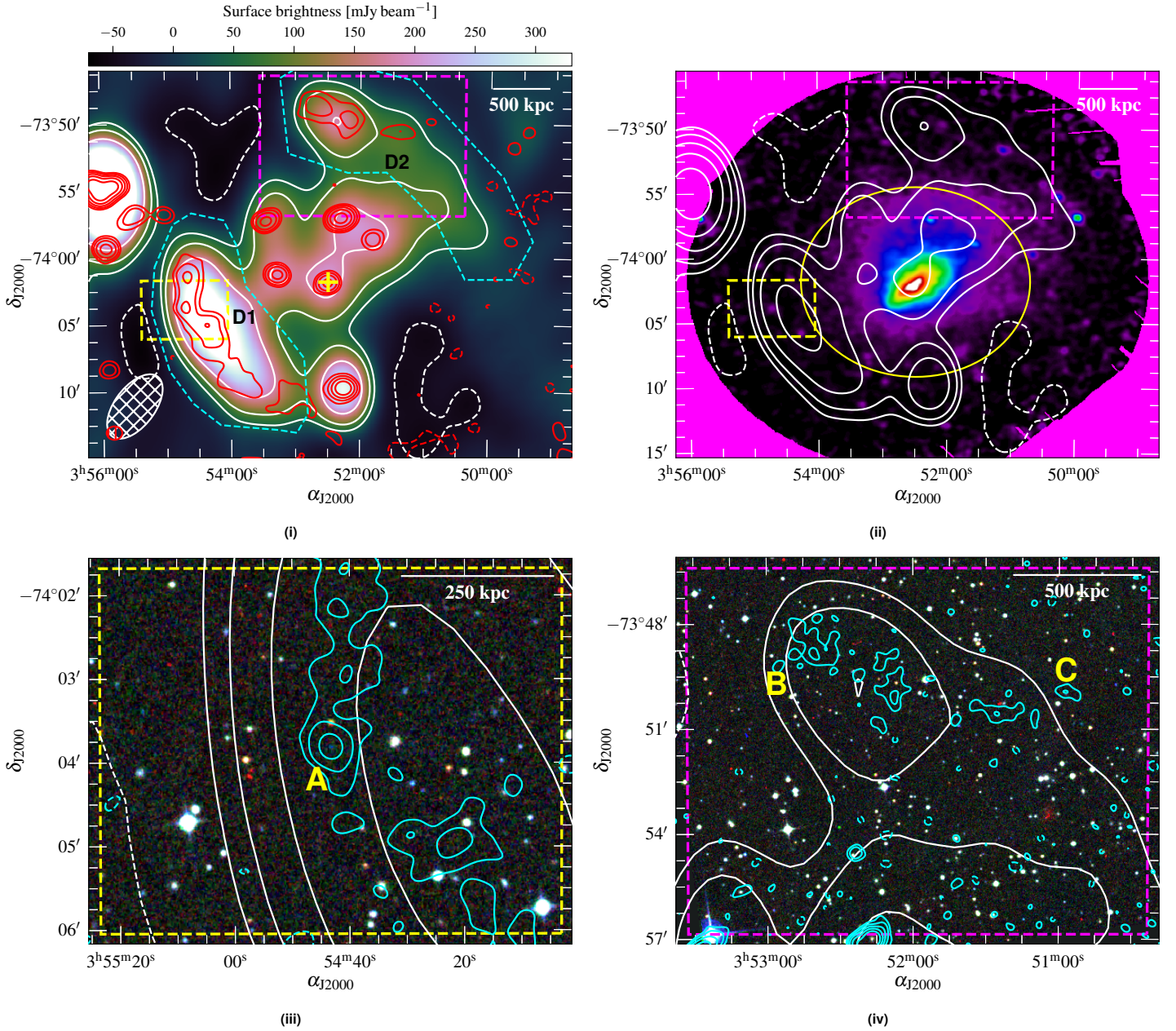


Figure 16. *Abell 3186.* (i) Background: MWA-2, 88-MHz, robust +2.0 image. (iii) and (iv) Background: RGB SSS image (*i, r, b*). (ii). Background: smoothed XMM-Newton EPIC image. The white contours are as in Fig. 2(i) for the background of (i) (with $\sigma_{\text{rms}} = 15 \text{ mJy beam}^{-1}$). Red contours: deep ASKAP low-resolution image, $[\pm 3, 6, 12, 24, 48] \times \sigma_{\text{rms}}$ ($\sigma_{\text{rms}} = 0.70 \text{ mJy beam}^{-1}$). Cyan contours: deep ASKAP robust +0.25, $[\pm 3, 6, 12, 24, 48] \times \sigma_{\text{rms}}$ ($\sigma_{\text{rms}} = 0.32 \text{ mJy beam}^{-1}$ and $\sigma_{\text{rms}} = 0.25 \text{ mJy beam}^{-1}$ for (iii) and (iv), respectively). Other image features are as in Fig. 2 and Fig. 3, with the magenta box indicating the location of (iv) on (i) and (ii).

source sits between two X-ray clumps. We find the spectral index to be $\alpha_{88}^{200} = -1.8 \pm 0.4$ (Fig. 26(xxiii)), and suggest the source is fossil plasma or otherwise a remnant radio galaxy.

3.1.8. FIELD10

Abell 3164. (Fig. 21). MWA and the VAST data reveal a complex radio galaxy with at least three distinct remnant components (D1–3 in Fig. 21(i)) with LASs 3.5, 3.8, and 3.1 arcmin and LLSs of 240, 260, and 210 kpc for D1–3, respectively. The head-tail (HT) galaxy (hosted by FAIRALL 0757; Fairall 1984) in the cluster is

clearly connected to D3 and is likely responsible for at least D2, however, it is not clear whether D1 has spawned from the same galaxy. The source-subtracted VAST data is shown in Fig. 21(i) and highlights the steepness of D2. After subtraction of Sources A and B from the relevant measurements, we obtain spectral indices of D1: $\alpha_{88}^{887} = -1.48 \pm 0.08$ (Fig. 26(xxiv)), D2: $\alpha_{88}^{216} = -2.3 \pm 0.1$ (though Fig. 26(xxv) shows some curvature within the MWA band, and D2 is also fit with a generic curved model between 88–887.5 MHz), D3: $\alpha_{154}^{887} = -1.78 \pm 0.07$ (Fig. 26(xxvi)). We do not believe significant flux density is missing, since D1, which is comparative

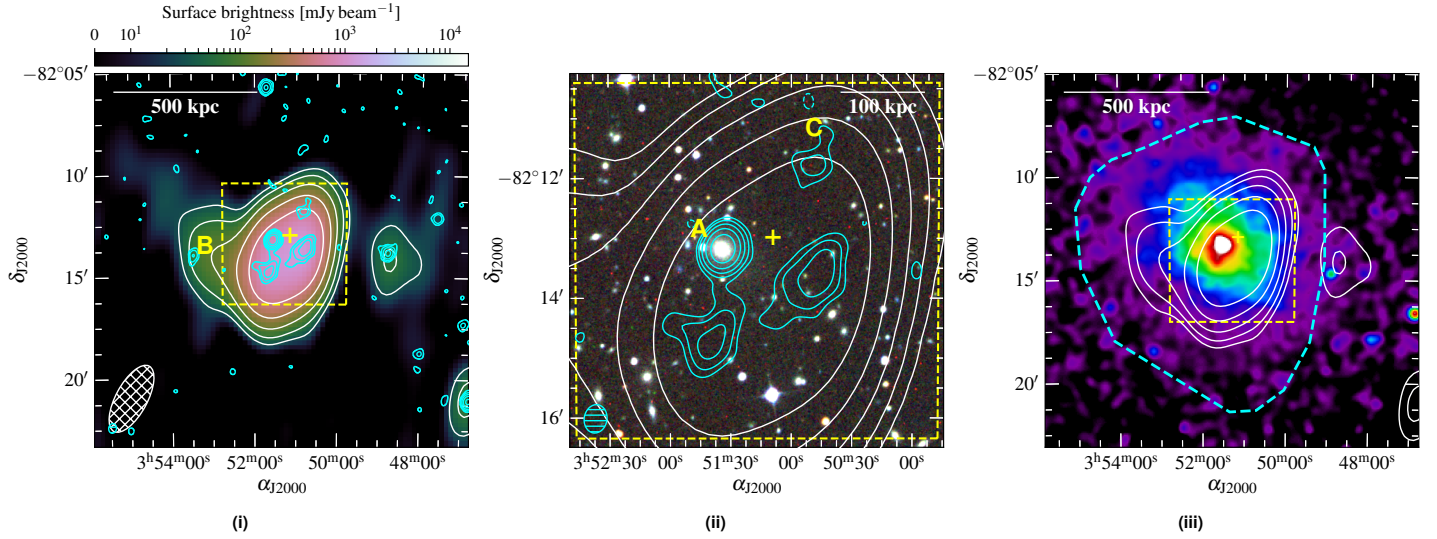


Figure 17. *Abell S0405.* (i) Background: MWA-2, 154-MHz, robust +2.0 image. (ii) Background: RGB SSS image (*i, r, b*). (iii). Background: smoothed *Chandra* image. The white contours are as in Fig. 2(i) for the background of (i) (with $\sigma_{\text{rms}} = 10 \text{ mJy beam}^{-1}$). Cyan contours: RACS survey image, $[\pm 3, 6, 12, 24, 48] \times \sigma_{\text{rms}}$ ($\sigma_{\text{rms}} = 0.28 \text{ mJy beam}^{-1}$). Other image features are as in Fig. 2.

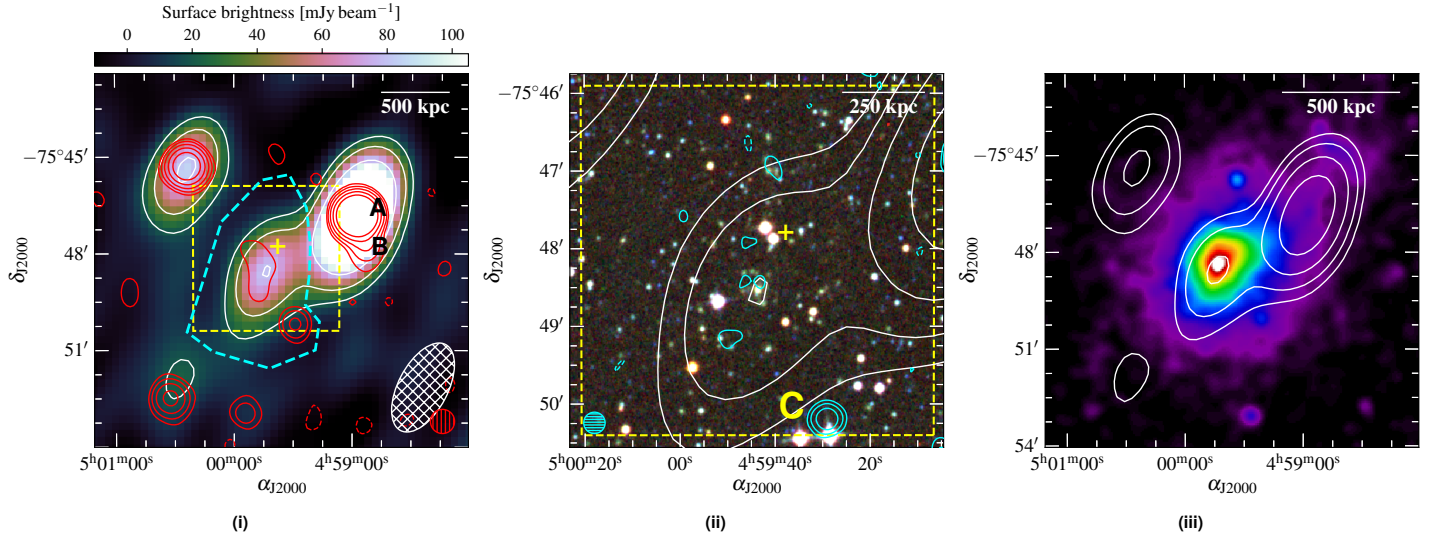


Figure 18. *PSZ1 G287.95–32.98.* (i) Background: MWA-2, 154-MHz, robust +2.0 image. (ii) Background: RGB SSS image (*i, r, b*). (iii). Background: smoothed XMM-Newton image. The white contours are as in Fig. 2(i) for the background of (i) (with $\sigma_{\text{rms}} = 6.6 \text{ mJy beam}^{-1}$). Red contours: RACS low resolution image $[\pm 3, 6, 12, 24, 48] \times \sigma_{\text{rms}}$ ($\sigma_{\text{rms}} = 0.25 \text{ mJy beam}^{-1}$). Cyan contours: RACS robust +0.25 image, $[\pm 3, 6, 12, 24, 48] \times \sigma_{\text{rms}}$ ($\sigma_{\text{rms}} = 0.15 \text{ mJy beam}^{-1}$). Other image features are as in Fig. 2.

in angular scale, is recovered consistently alongside the MWA. We see steepening from D3–D2, but D1 is flatter, which suggests either (1) it may not be associated with past episode from the HT or (2) it has been re-accelerated/revived by ICM motion. Steepening of the spectrum of HT radio galaxies is observed to increase with distance from the host galaxy (e.g. the HT in Abell 1132; Wilber et al. 2018, or in Abell 1775; Botteon et al. 2021a).

The smoothed RASS image is shown in Fig. 21(iii) which highlights a faint X-ray structure detected as the cluster, elongated towards the SE. The X-ray emission does not elucidate the nature of the diffuse components based on location, however, the diffuse emission resides within the clearly elongated X-ray emission to the south of the cluster, thus is in a region where we can assume

dynamical activity is occurring.

3.1.9. FIELD11

Abell 3365. (Fig. 22). Abell 3365 (RXJ 0548.8–2154) was reported to host a relic and candidate second relic by van Weeren et al. (2011)—at the time, spectral coverage was minimal. While not in our original survey scope, the cluster resides at the edge of a field that was opportunistically processed for other targets. We show the 154-MHz map in Fig. 22 with RACS contours overlaid. The NE relic is detected (D1), and the SW candidate relic source is also detected (D2). An additional extension, labelled D3, is also detected that has not been identified in other radio maps. We utilise the additional spectral coverage offered by the MWA-2 and find,

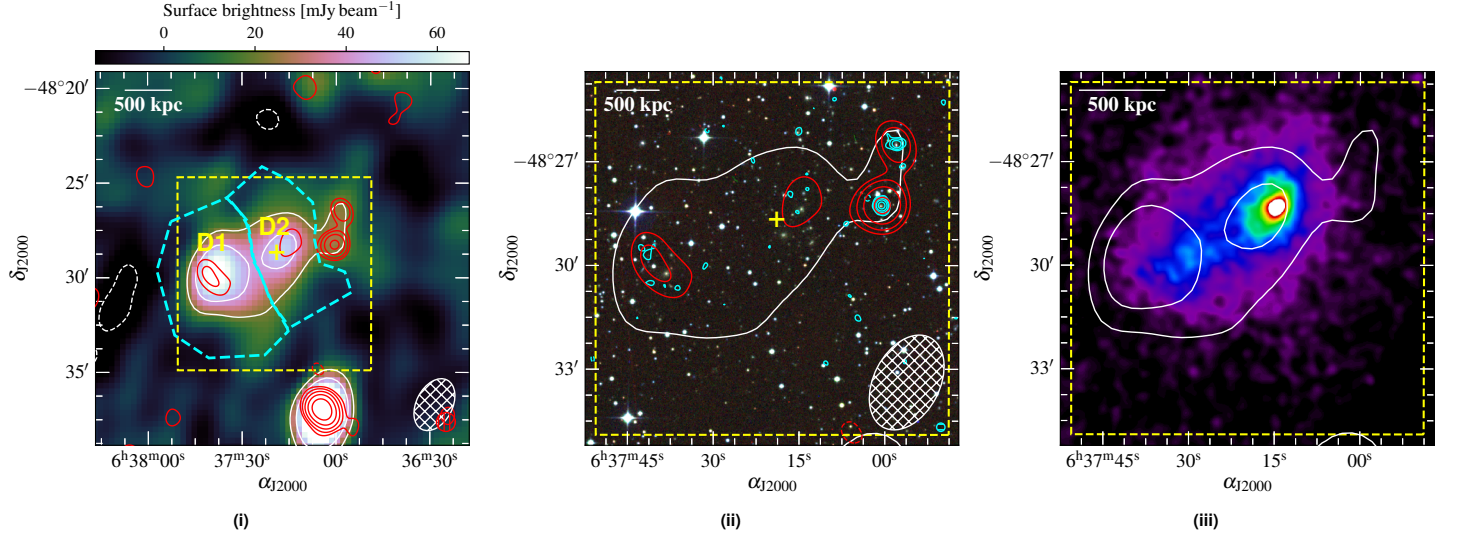


Figure 19. Abell 3399. (i) Background: MWA-2, 118-MHz, robust +2.0 image. (ii) Background: RGB SSS image (*i, r, b*). (iii). Background: smoothed *Chandra* image. The white contours are as in Fig. 2(i) for the background of (i) (with $\sigma_{\text{rms}} = 7.3 \text{ mJy beam}^{-1}$). Red contours: RACS discrete source-subtracted image, $[\pm 3, 6, 12, 24, 48] \times \sigma_{\text{rms}}$ ($\sigma_{\text{rms}} = 0.45 \text{ mJy beam}^{-1}$). Cyan contours: RACS survey image, $[\pm 3, 6, 12, 24, 48] \times \sigma_{\text{rms}}$ ($\sigma_{\text{rms}} = 0.17 \text{ mJy beam}^{-1}$). Other image features are as in Fig. 2.

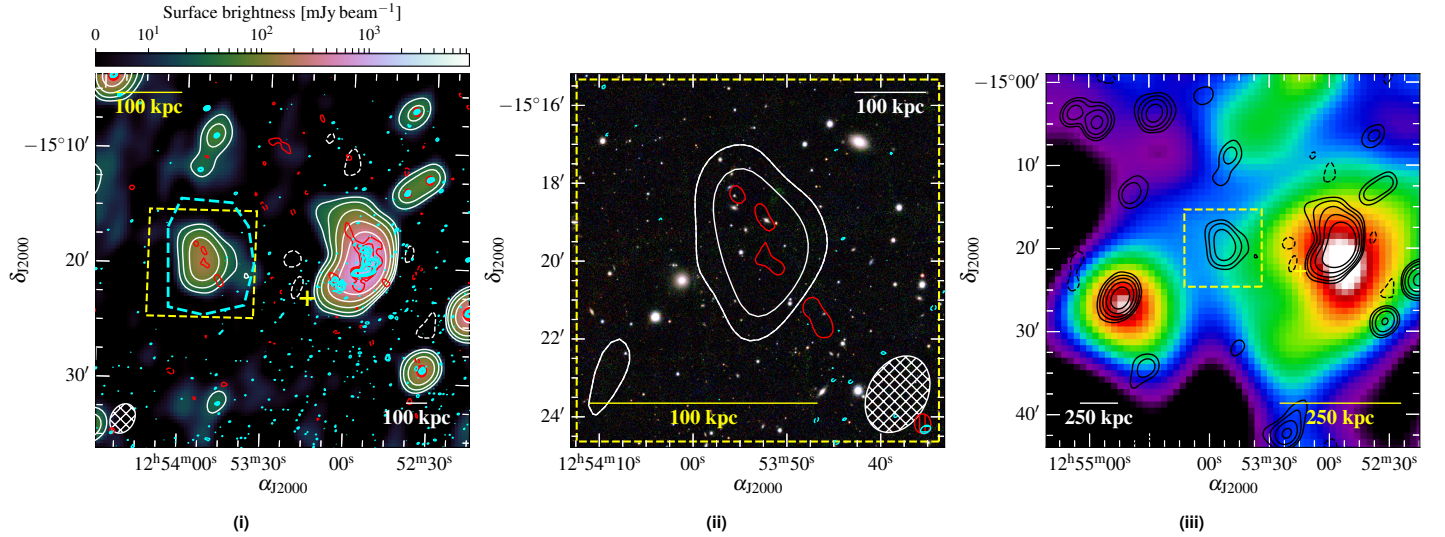


Figure 20. MCXC J1253.2–1522 (Abell 1631). (i) Background: MWA-2, 118-MHz, robust +2.0 image. (ii) Background: RGB PS1 image (*i, r, g*). (iii). Background: smoothed RASS image. The white (black) contours are as in Fig. 2(i) for the background of (i) (with $\sigma_{\text{rms}} = 7.0 \text{ mJy beam}^{-1}$). Red contours: TGSS image, $[\pm 3, 6, 12, 24, 48] \times \sigma_{\text{rms}}$ ($\sigma_{\text{rms}} = 3.5 \text{ mJy beam}^{-1}$). Cyan contours: RACS survey image, $[3, 6, 12, 24, 48] \times \sigma_{\text{rms}}$ ($\sigma_{\text{rms}} = 0.32 \text{ mJy beam}^{-1}$). Other image features are as in Fig. 2, with the addition of a separate, yellow linear scale at the redshift of Abell 1631.

after subtraction of Source A, a power law model for the NE relic, with $\alpha_{\text{D1},88}^{1420} = -0.85 \pm 0.03$ (Fig. 26(xxvii)). We note a curious feature of the flux density measurements wherein the lower MWA bands separate from the higher bands—we cannot explain this feature as either instrumental or physical. While the relic is detected in the RACS data, we note significant negative bowls around the source indicating a lack of flux recovery. A lower limit is provided but not used in fitting. The resultant spectral shape is reasonably shallow for a relic. The SW relic (D2) is detected in MWA-2 data as well, but is too confused in the 88-MHz band. The resultant SED provides $\alpha_{\text{D2},118}^{1420} = -0.76 \pm 0.08$ (Fig. 26(xxviii)), noting that the discrete Source A discussed by van Weeren et al. (2011) is not

confused in these bands and is not required to be subtracted.

Golovich et al. (2019) present deep *XMM-Newton* observations of the cluster along with spectro-optical analysis (see their Fig. 25), highlighting the merger axis and location of the candidate SW relic with respect to three subclusters within the system. They note there is no distinct alignment of the subclusters with the W relic candidate (D2), and given the shallow spectrum we suggest this is not a relic source.

Despite this, Urdampilleta et al. (2021) find significant temperature jumps across both relics, finding evidence for shocks with Mach numbers $\mathcal{M}_{\text{west}} = 3.9 \pm 0.8$ and $\mathcal{M}_{\text{east}} = 3.5 \pm 0.6$, which for DSA may produce relics with flatter spectral indices as observed

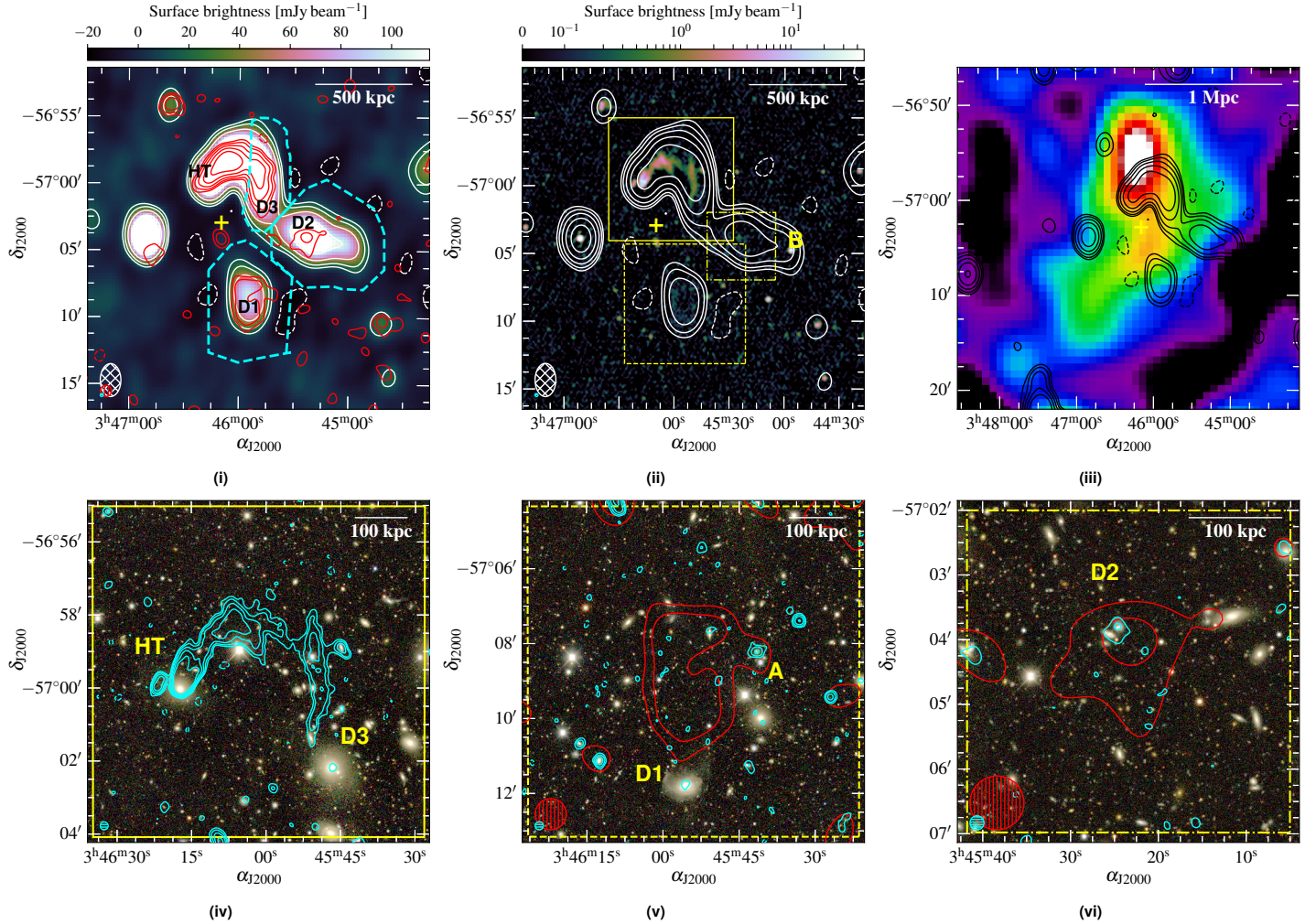


Figure 21. *Abell 3164*. Background: MWA-2, 154-MHz, robust +2.0 image. (ii) Background: VAST robust 0.0 image. (iii) Background: smoothed, RASS image. (iv)–(vi) Background: RGB DES image (*i*, *r*, *g*). The white contours are as in Fig. 2(i) for the background of (i) (with $\sigma_{\text{rms}} = 4.3 \text{ mJy beam}^{-1}$). Red contours: VAST source-subtracted image, $[\pm 3, 6, 12, 24, 48] \times \sigma_{\text{rms}}$ ($\sigma_{\text{rms}} = 0.17 \text{ mJy beam}^{-1}$). Cyan contours: VAST robust 0.0 image, $[\pm 3, 6, 12, 24, 48] \times \sigma_{\text{rms}}$ ($\sigma_{\text{rms}} = 0.09 \text{ mJy beam}^{-1}$). Other image features are as in Fig. 2. Yellow boxes on (ii) indicate the locations of (iv)–(vi).

here. Assuming DSA for these relics, and assuming $\alpha_{\text{integrated}} = \alpha_{\text{inj}}$ as might be the case for a re-accelerated fossil electron population (e.g. van Weeren et al., 2016), we find radio Mach numbers of $\mathcal{M}_{\text{RW}} = 4.2 \pm 0.4$ and $\mathcal{M}_{\text{RE}} = 2.5 \pm 0.1$ for the western and eastern relics, respectively. If accelerated from the thermal pool, we would expect $\alpha_{\text{inj}} = \alpha_{\text{integrated}} + 0.5$, resulting in a non-physical Mach number under standard DSA. The nature of both sources (D1 and D2) is uncertain.

Abell 0550. (Fig. 23). We report the detection of a large-scale, elongated emission structure on the periphery of Abell 0550 (Fig. 23(i)) with an LAS of ~ 15 arcmin (LLS ≈ 1.6 Mpc). We detect the source between 88–154 MHz in the MWA-2 data. We note that there is a spiral galaxy (WISEA J055346.34–211119.6, no redshift) near the centre of the emission, shown in Fig. 23(ii), denoted with an ‘S’. Spiral galaxies rarely host large-scale radio lobes, though a small number have been detected, sometimes with remnant lobes (e.g. Hota et al., 2011) and this may be such an example. With no compact emission detected in RACS from the spiral galaxy, we

can rule out significant AGN contribution and suggest the emission seen in the NVSS and MWA-2 images is related to star-formation processes and that the galaxy, if the host, is not actively fuelling the lobes, consistent with a steep spectrum. The resultant spectrum (Fig. 26(xxix)), with the spiral and compact Source A subtracted flattens at 1.4 GHz, and is fit with a generic curved power law, though the physical interpretation of this is not clear. New kpc-scale jets from the spiral that are not subtracted may contribute to the spectral flattening, though this is unlikely to be so extreme and we suggest residual flux from the extended emission from the spiral is affecting the measurements. Across the MWA band we fit a power law model finding a spectral index of $\alpha_{88}^{154} = -2.4 \pm 0.3$. Fig. 23(iii) shows the emission with respect to the X-ray-emitting core of the cluster, though the source is at the edge of the X-ray data. Bernardi et al. (2016) observed the cluster with KAT-7, searching for a central radio halo. This elongated source is outside of their observed FoV but a halo was not detected, and the data here (MWA-2 and re-processed RACS) do not suggest the presence of a halo either.

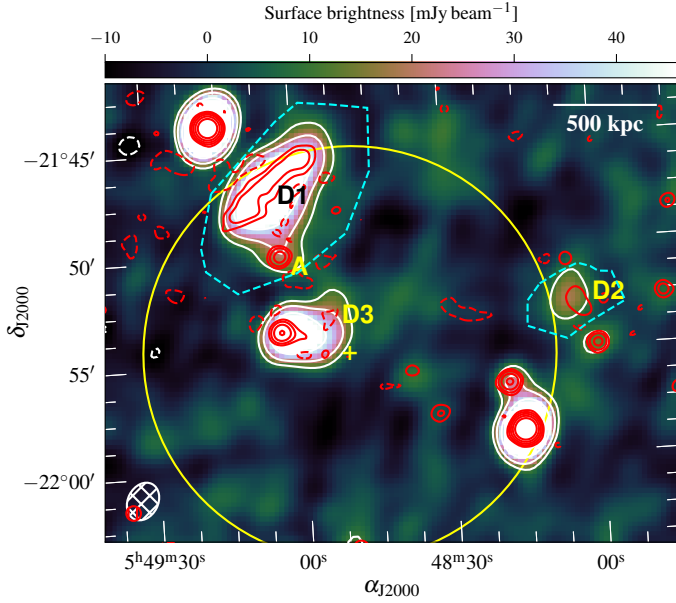


Figure 22. Abell 3365. Background: MWA-2, 154-MHz, robust +1.0 image. The white contours are as in Fig. 2(i) for the background image (with $\sigma_{\text{rms}} = 3.5 \text{ mJy beam}^{-1}$). Red contours: RACS low-resolution, $[\pm 3, 6, 12, 24, 48] \times \sigma_{\text{rms}}$ ($\sigma_{\text{rms}} = 0.47 \text{ mJy beam}^{-1}$). Other image features are as in Fig. 2 and Fig. 3. Note the white circle has a 1 Mpc radius, centered on the coordinates associated with RXC J0548.8–2154 (i.e. the X-ray component for the system).

4. Discussion

4.1. Low frequency radio halos and relics

Scaling relationships between diffuse source radio luminosity and cluster properties (e.g. M_{500}) have been established for halos, mini-halos, and relics. Recent works have shown that for radio halos these relationships are converging at 1.4 GHz and 150 MHz (Cuciti et al., 2021; van Weeren et al., 2021; Duchesne et al., 2021c). For relics this is less certain as confirmed radio relic numbers remain low, and scaling relations here typically utilise double relic detections (e.g. de Gasperin et al., 2014, 2015; Duchesne et al., 2021a). Similar relationships are found for mini-halos (e.g. Giacintucci et al., 2019; Richard-Laferrrière et al., 2020), though the effect of the CC on cluster properties (e.g. mass) and contribution of the radio-loud BCG on the estimated mini-halo power may create additional uncertainty in the relations (e.g. Richard-Laferrrière et al., 2020).

Despite scatter in these relations, sources in each class tend to stay near the currently determined fits. As a point of comparison, we plot a selection of our sources (namely, candidate halos, relics, and some of the miscellaneous fossil sources) on the P_ν – M_{500} planes to compare against the larger samples. Fig. 24 shows these relations for halos (Fig. 24(i) and Fig. 24(ii)) and relics (Fig. 24(iii) and Fig. 24(iv)) for $\nu \in \{150, 1400\}$ MHz. For each, we plot the best-fit relations from Duchesne et al. (2021c) and Duchesne et al. (2021a) for halos and relics, respectively. Additionally, the full literature samples used in those works are plotted, and the P_{150} – M_{500} relation for double relics is scaled from 1400 MHz following Equation 6 from Duchesne et al. (2021c), assuming a mean spectral index of $\alpha = -1.2$.

As expected, at 150 MHz the candidate USSRHs in Abell 2811 and PSZ1 G287.95–32.98 shift to be placed on the orthogonal regression line. This is largely consistent with the USSRH population (e.g. Cassano et al., 2013; Bruno et al., 2021; Duchesne et al., 2021c) which are normally found to be under-luminous with respect to the 1400 MHz scaling relations but shift towards the regression line when the relation is computed at 150 MHz. Conversely, the candidate halo (or point source) in Abell 2693 sits far above both relations, though the derived mass approaches the limits obtainable with RASS and carries significant uncertainty. Given how few halos are detected in low mass clusters ($\lesssim 5 \times 10^{14} M_\odot$) and our lack of understanding in this low-mass regime it is difficult to rule out the radio halo classification, however, as discussed previously other characteristics (e.g. location) are less consistent with a halo interpretation. While we suggest the sources in Abell 3164 are fossil plasma sources, their nature is still somewhat uncertain and D1 and D2 are included on Fig. 24(iii) and Fig. 24(iv) as a reference.

4.2. Clues from integrated spectra—seed electrons & palaeontology

4.2.1. Cluster diffuse sources samples

We find that of the 31 sources reported in this survey²⁴, that 13 are likely fossil radio plasma sources: remnant radio galaxies or otherwise remnant outflows from AGN at unknown stages after cessation of an episode of nuclear activity. These sources are labelled ‘F’ and ‘r’ in Table 1. For classification purposes, in Table 1 remnant (‘r’) is used when the morphology still resembles a radio galaxy and when a possible host is identified. These sources are unlikely to be radio halos or relics based on largely morphological and other physical characteristics.

Having established this sample we wish to consider how fossil radio plasmas relate to other diffuse cluster emission. In particular, we wish to consider the question of whether these sources provide a link between the source of electrons in the ICM from which relics and halos may be generated. With the MWA (and ASKAP) we are able to obtain estimates of the spectral index in the MHz regime where most emission models retain power law shapes, and comparisons between different classes of sources (fossils, halos, relics, and remnant radio galaxies) will not be overly effected by spectral curvature.

Table 4 presents details of a literature sample of integrated spectral indices for populations of halos (H), relics (R), mini halos (mH), remnants (r), and cluster-based fossil sources (F), which we compare to our cluster remnant and fossil sample. Where available, we use spectral indices derived from low-frequency measurements (i.e. within the MWA band, ~ 150 MHz up to ~ 1 GHz).

Spectral indices have been derived from a variety of measurements/instruments and spectra may steepen (if a low-frequency observation is more sensitive; e.g. Macario et al., 2010) or flatten (if a high-frequency observation is more sensitive; e.g. Ogrean et al., 2015) artificially due to a mismatch of u, ν sampling and general sensitivity between observations. This introduces further

²⁴Including candidate sources, and radio galaxies/point sources discussed in Section 3.1.

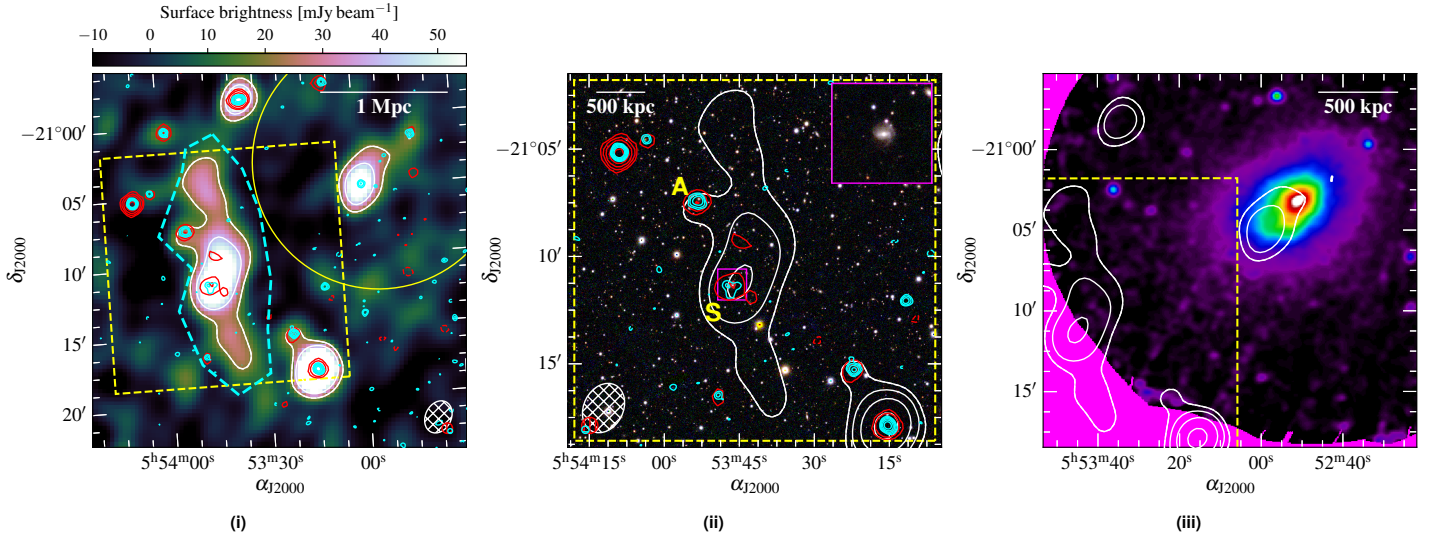


Figure 23. Abell 0550. Background: MWA-2, 118-MHz, robust +1.0 image. (ii) Background: RGB PS1 image (*i*, *r*, *g*). (iii) Background: smoothed XMM-Newton EPIC image. The white contours are as in Fig. 2(i) for the background of (i) (with $\sigma_{\text{rms}} = 6.6 \text{ mJy beam}^{-1}$). Red contours: NVSS image, $[\pm 3, 6, 12, 24, 48] \times \sigma_{\text{rms}}$ ($\sigma_{\text{rms}} = 0.57 \text{ mJy beam}^{-1}$). Cyan contours: RACS robust +0.25 image, $[\pm 3, 6, 12, 24, 48] \times \sigma_{\text{rms}}$ ($\sigma_{\text{rms}} = 0.25 \text{ mJy beam}^{-1}$). Other image features are as in Fig. 2 and Fig. 3. Note (iii) clips at the location of relic as that is the FoV of the XMM-Newton observation.

Table 4 Median spectral indices for the diffuse source populations.

Type	Number	med(α)	Ref. ^a
R	46	-1.2 ± 0.2	(a),(b)
H	35	-1.3 ± 0.3	(c)
mH	12	-1.2 ± 0.1	(d)
r (field)	35	-0.9 ± 0.2	(e),(f),(g)
r (cluster)	6	-1.8 ± 0.4	(h)
F	21	-1.7 ± 0.4	(b),(i),(j),(k),(l)
r/F	13	-1.7 ± 0.4	this work

^a Samples drawn from: (a) Duchesne et al. (2021a); (b) van Weeren et al. (2019); (c) Duchesne et al. (2021c); (d) Richard-Laferrière et al. (2020); (e) Brienza et al. (2017); (f) Mahatma et al. (2018); (g) Quici et al. (2021); (h) Murgia et al. (2011); (i) Duchesne et al. (2020); (j) Mandal et al. (2020); (k) Giacintucci et al. (2020); (l) Hodgson et al. (2021).

uncertainty to the spectral indices, but is not likely to bias the distributions significantly towards steeper or flatter spectra.

We show the histograms of reported α in Fig. 25 for our sample of cluster fossil plasma sources (r and F in Table 1) against three classes of objects from the samples described in Table 4: i) halos and mini halos, ii) relics (both single and double systems), and iii) cluster fossils sources and both field and cluster remnants.

Median α obtained for each distribution are reported in Table 4. We note the single relic population is unlikely to be fundamentally different to the double relic population, which are thought to form through the same shock-acceleration processes. This is evident in Fig. 25(ii) which shows the distribution of α is not significantly different between the two samples. Furthermore, the halo and relic median spectral indices are consistent, suggesting a common generation time if drawn from the same underlying electron population

(though as discussed previously the generation mechanisms are thought to be different, but both associated with mergers). We note that the radio halo sample shown in Fig. 25(i) includes USSRHs as expected from turbulent (re-)acceleration processes which creates a significant tail in the distribution towards steeper spectra. Relics show a similar ultra-steep-spectrum tail but are much more densely peaked around their median value.

4.2.2. Remnants, fossils, and revived radio plasma: seed electron populations?

Fig. 25 shows that, in general, fossil plasma sources tend towards steeper spectra than the relic and halo populations, and are significantly steeper than field remnant radio galaxies. The few remnants found in clusters (e.g. Murgia et al., 2011) typically have steeper spectra at equivalent frequencies than their field counterparts²⁵. Sources such as D1 in Abell S1099 may represent a younger cluster remnant, and with no evidence of morphological disturbance of the ICM we do not consider this a re-accelerated source. It is likely the cluster environment plays a role in allowing these sources to remain visible for longer (e.g. by constraining diffusion of the electrons into the surrounding ICM; Murgia et al. 2011). Studies (Brienza et al., 2017; Mahatma et al., 2018; Jurlin et al., 2020; Quici et al., 2021) suggest remnants have a short observable lifetime before surface brightness becomes prohibitively faint as the plasma both steepens in spectrum and expands. With low numbers of these remnant and fossil sources, it is difficult to draw firm conclusions about the role of the cluster environment.

Given the ubiquity of radio galaxies of complex morphologies in clusters (e.g. Hardcastle & Sakelliou, 2004; Clarke & Ensslin, 2006; Sakelliou et al., 2008; Botteon et al., 2020c; Brüggen et al., 2021)

²⁵Note also Parma et al. (2007) reports a small number of remnants within cluster environments, though their sample was taken from sources with $\alpha < -1.3$ so by construction they are steeper than remnants found in recent searches.

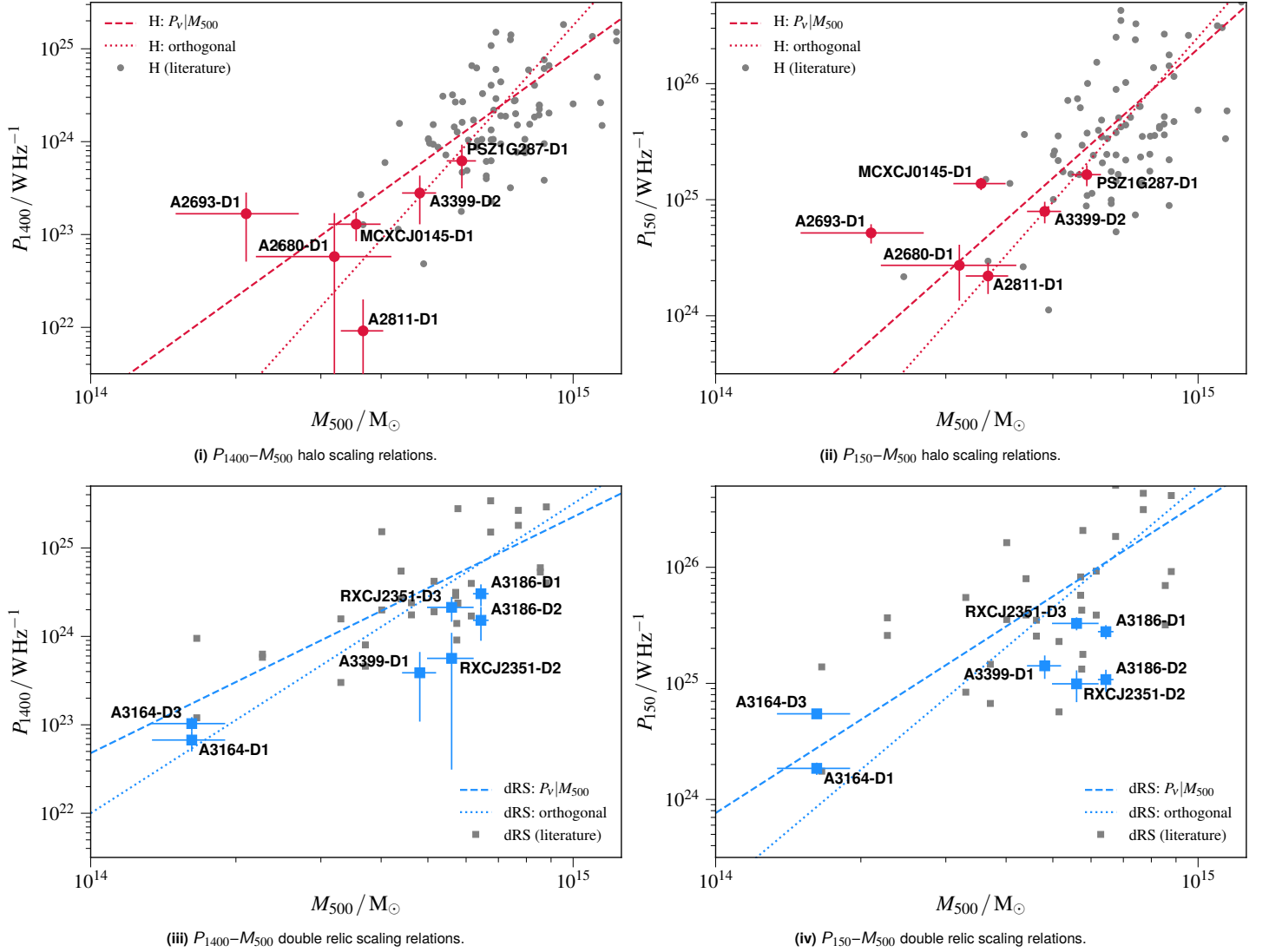


Figure 24. Halo and double relic P_V – M_{500} scaling relations with candidate sources from this work overlaid. Best-fit lines are also shown from Duchesne et al. (2021a) for relics, with scaling to 150 MHz, and Duchesne et al. (2021c) for halos. Literature data as discussed in Duchesne et al. (2021a) and Duchesne et al. (2021c) are also shown for reference. $P_V|M_{500}$ refers to fits determined assuming P_V is the dependent variable and M_{500} the independent variable, and ‘orthogonal’ refers to an orthogonal regression using the Bivariate Correlated Errors and intrinsic Scatter method (BCES; Akritas & Bershady, 1996)—see Duchesne et al. (2021c) for further BCES fitting details.

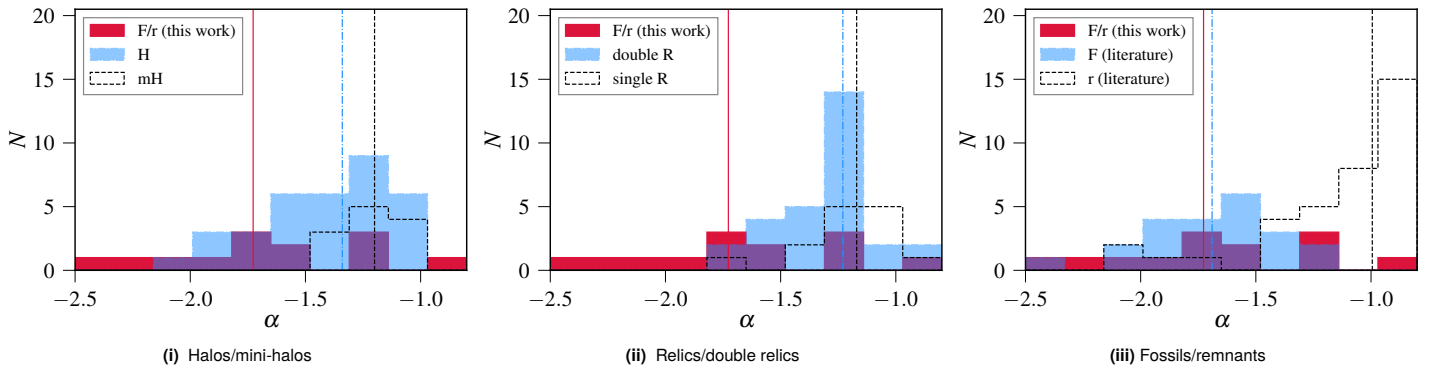


Figure 25. Spectral index distributions for (i) radio halos, (ii) relics (double and single), and (iii) remnant radio galaxies and fossil radio plasma sources, compared to the collection of fossils plasma sources reported in this work. See Section 4.2 and Table 4 for population details. Vertical lines indicate median population values. Note that bins are clipped at $-2.5 \geq \alpha \geq -0.8$, and our sample is generally clipped at ~ -0.9 by construction due to the original search criteria.

we expect a large population of these fossil plasma sources waiting to be re-accelerated by merger-based shocks and turbulence. By construction, we have steep-spectrum (and ultra-steep-spectrum) sources in either relaxed, or ‘ambiguously dynamic’ clusters that cannot be described as relics or halos—these are likely fossil radio plasma and highlight a population of sources in clusters that can provide seed electrons for relic and halo sources as well as smaller-scale revived fossil plasma like phoenixes.

Examples exist in the literature of re-acceleration of fossil plasmas with some connection to AGN (e.g. Bonafede et al., 2014; van Weeren et al., 2017; de Gasperin, 2017; Wilber et al., 2019), and simulations have shown that fossil electrons from AGN outflows and long-dead radio galaxies can (1) exist diffusively within the ICM (Vazza et al., 2021) and (2) be re-accelerated by normal DSA-like processes (e.g. Kang, 2018). It is not clear that the acceleration efficiency for electrons at shocks is sufficient to produce the observed relics unless there is a mildly-relativistic population (e.g. Botteon et al. 2020b), though many observed properties of relics do not require a population of fossil electrons (e.g. Rajpurohit et al., 2020, 2021b). The distribution of α for relics and halos extends into the ultra-steep-spectrum regime which would be consistent with a population of re-accelerated fossil electrons in low-energy events (e.g. from weak mergers triggering USSRH; Brunetti et al. 2008), though it is not clear whether the density of such a fossil electron population would be sufficient to produce the observed emission. In general, such weaker events should be more common and simulations suggest a large population of faint diffuse sources should exist (e.g. Nuza et al., 2012); however, these low surface brightness and ultra-steep spectrum sources are still challenging to detect and image. Surveys with e.g. LOFAR (especially combining HBA and LBA data for spectral information) should uncover a larger number of these ultra-steep-spectrum sources and indeed instruments like MWA, LOFAR, and the uGMRT are now starting to uncover them (e.g. Giacintucci et al., 2020; Mandal et al., 2020; Hodgson et al., 2021).

5. Summary

In this work we have reported an MWA-2 follow-up survey of candidate diffuse cluster radio sources originally detected in MWA Phase I data as part of the GLEAM survey and EoR0 field survey (D21). We have combined the MWA-2 data with recent ASKAP data at 887 MHz to (1) attempt to classify the sources based on their morphologies, host cluster properties, and SEDs and (2) simply ensure sources are not confused point sources—an ongoing problem with low-resolution interferometric observations. We report on 31 sources, with 6 candidate halos, 2 mini-halos (1 candidate), 3 relics (1 candidate and 1 double relic system), 13 remnant AGN or miscellaneous fossil plasmas. Some of the candidate sources are found to be point sources or radio galaxies, and we also follow-up the ‘twin relic’ in Abell 0168 reported by Dwarakanath et al. (2018) and the double-relic system in Abell 3365 reported by van Weeren et al. (2011). Specifically, we report the detection of a new double relic system associated with Abell 3186, a mini-halo associated with RXC J0137.2–0912 and that the candidate halo in Abell 2811 reported by D21 has a spectral index of $\alpha = -2.5 \pm 0.4$, though this

will require follow-up high resolution, high-sensitivity observations to confirm its nature. We also observe an HT galaxy in Abell 3164 that exhibits episodic activity with a potentially re-accelerated component.

We find that generally the relics and halos presented here sit in reasonable locations on the established $P_{1400}-M_{500}$ and $P_{150}-M_{500}$ scaling relations, with the USSRHs shifting closer towards the $P_{150}-M_{500}$ relation. We also compare the integrated spectra of our sample of cluster fossil and remnant sources against various samples of steep-spectrum, diffuse cluster sources as well as field remnant radio galaxies, finding that the general spectral properties are consistent with the literature fossil radio source population. This is in turn consistent with the integrated, low-frequency spectral indices of cluster-based remnant radio galaxies. We have discussed the putative link between these fossil sources and other diffuse cluster sources, noting that the distributions of spectral indices for diffuse clusters sources would be consistent with fossil radio plasmas as seed electrons for the emission.

In this work we have just gently brushed the dust off of a small collection of old fossils and large-scale, deep, and high-resolution surveys with the SKA pathfinders—particularly ASKAP and MeerKAT with $\sim 5-15$ arcsec resolution over the Southern Sky—will enable high-fidelity follow-up of these types of sources placing constraints on the ≥ 1 GHz spectrum. In the future SKA should dig deeper, revealing myriad new ultra-steep spectrum radio fossils, providing key observational evidence for any link between these sources and cluster halos and relics.

Acknowledgements. We would like to thank an anonymous referee for their useful feedback. The authors would like to thank Dr. Paula Tarrío Alonso for providing mass estimates for Abell 2680 and Abell 2693. SWD acknowledges an Australian Government Research Training Program scholarship administered through Curtin University. The Australian SKA Pathfinder is part of the Australia Telescope National Facility which is managed by CSIRO. Operation of ASKAP is funded by the Australian Government with support from the National Collaborative Research Infrastructure Strategy. ASKAP uses the resources of the Pawsey Supercomputing Centre. Establishment of ASKAP, the Murchison Radio-astronomy Observatory and the Pawsey Supercomputing Centre are initiatives of the Australian Government, with support from the Government of Western Australia and the Science and Industry Endowment Fund. We acknowledge the Wajarri Yamatji people as the traditional owners of the Observatory site. Support for the operation of the MWA is provided by the Australian Government (NCRIS), under a contract to Curtin University administered by Astronomy Australia Limited. This research has made use of data obtained from the *Chandra* Data Archive and the *Chandra* Source Catalog, and software provided by the *Chandra* X-ray Center (CXC) in the application package *CIAO*. This research has made use of the NASA/IPAC Extragalactic Database (NED), which is operated by the Jet Propulsion Laboratory, California Institute of Technology, under contract with the National Aeronautics and Space Administration. This research has made use of the VizieR catalogue access tool, CDS, Strasbourg, France. The original description of the VizieR service was described in Ochsenbein et al. (2000).

This research made use of a number of python packages not explicitly mentioned in the main text: *aplpy* (Robitaille & Bressert, 2012), *astropy* (Astropy Collaboration et al., 2013), *matplotlib* (Hunter, 2007), *numpy* (van der Walt et al., 2011) and *scipy* (Jones et al., 2001).

References

- Abbott T. M. C., et al., 2018, *ApJS*, **239**, 18
- Abell G. O., 1958, *ApJS*, **3**, 211
- Abell G. O., Corwin Jr. H. G., Olowin R. P., 1989, *ApJS*, **70**, 1
- Akritis M. G., Bershadsky M. A., 1996, *ApJ*, **470**, 706
- Astropy Collaboration et al., 2013, *A&A*, **558**, A33
- Bagchi J., et al., 2011, *ApJ*, **736**, L8
- Bartalucci I., et al., 2017, *A&A*, **608**, A88
- Bernardi G., et al., 2016, *MNRAS*, **456**, 1259
- Bock D. C.-J., Large M. I., Sadler E. M., 1999, *AJ*, **117**, 1578
- Bogdán Á., et al., 2013, *ApJ*, **772**, 97
- Böhringer H., et al., 2004, *A&A*, **425**, 367
- Böhringer H., et al., 2010, *A&A*, **514**, A32
- Bonafede A., et al., 2012, *MNRAS*, **426**, 40
- Bonafede A., Intema H. T., Brüggen M., Girardi M., Nonino M., Kantharia N., van Weeren R. J., Röttgering H. J. A., 2014, *ApJ*, **785**, 1
- Botteon A., Gastaldello F., Brunetti G., Dallacasa D., 2016a, *MNRAS*, **460**, L84
- Botteon A., Gastaldello F., Brunetti G., Kale R., 2016b, *MNRAS*, **463**, 1534
- Botteon A., et al., 2018, *MNRAS*, **478**, 885
- Botteon A., et al., 2020a, *MNRAS*, **499**, L11
- Botteon A., Brunetti G., Ryu D., Roh S., 2020b, *A&A*, **634**, A64
- Botteon A., et al., 2020c, *ApJ*, **897**, 93
- Botteon A., et al., 2021a, *A&A*, **649**, A37
- Botteon A., et al., 2021b, *ApJ*, **914**, L29
- Bourdin H., Mazzotta P., 2008, *A&A*, **479**, 307
- Bourdin H., Mazzotta P., Markevitch M., Giacintucci S., Brunetti G., 2013, *ApJ*, **764**, 82
- Bravi L., Gitti M., Brunetti G., 2016, *MNRAS*, **455**, L41
- Brienza M., et al., 2017, *A&A*, **606**, A98
- Briggs D. S., 1995, PhD thesis, The New Mexico Institute of Mining and Technology, Socorro, New Mexico, <http://www.aoc.nrao.edu/dissertations/dbriggs/>
- Brüggen M., et al., 2021, *A&A*, **647**, A3
- Brunetti G., Jones T. W., 2014, *International Journal of Modern Physics D*, **23**, 1430007
- Brunetti G., Vazza F., 2020, *Phys. Rev. Lett.*, **124**, 051101
- Brunetti G., Setti G., Feretti L., Giovannini G., 2001, *MNRAS*, **320**, 365
- Brunetti G., et al., 2008, *Nature*, **455**, 944
- Brunetti G., Cassano R., Dolag K., Setti G., 2009, *A&A*, **507**, 661
- Bruno L., et al., 2021, *A&A*, **650**, A44
- Buote D. A., 2001, *ApJ*, **553**, L15
- Caretta C. A., Maia M. A. G., Kawasaki W., Willmer C. N. A., 2002, *AJ*, **123**, 1200
- Cassano R., Ettori S., Giacintucci S., Brunetti G., Markevitch M., Venturi T., Gitti M., 2010, *ApJ*, **721**, L82
- Cassano R., et al., 2013, *ApJ*, **777**, 141
- Cavagnolo K. W., Donahue M., Voit G. M., Sun M., 2008, *ApJ*, **682**, 821
- Cavaliere A., Fusco-Femiano R., 1976, *A&A*, **49**, 137
- Chambers K. C., et al., 2016, preprint, ([arXiv:1612.05560](https://arxiv.org/abs/1612.05560))
- Chapman J. M., Dempsey J., Miller D., Heywood I., Pritchard J., Sangster E., Whiting M., Dart M., 2017, CASDA: The CSIRO ASKAP Science Data Archive. p. 73
- Chon G., Böhringer H., 2012, *A&A*, **538**, A35
- Clarke T. E., Ensslin T., 2006, *Astronomische Nachrichten*, **327**, 553
- Clarke T. E., Kronberg P. P., Böhringer H., 2001, *ApJ*, **547**, L111
- Cohen A. S., Clarke T. E., 2011, *AJ*, **141**, 149
- Condon J. J., Cotton W. D., Greisen E. W., Yin Q. F., Perley R. A., Taylor G. B., Broderick J. J., 1998, *AJ*, **115**, 1693
- Coziol R., Andernach H., Caretta C. A., Alamo-Martínez K. A., Tagó E., 2009, *AJ*, **137**, 4795
- Craddace R., et al., 2002, *ApJS*, **140**, 239
- Cuciti V., et al., 2021, *A&A*, **647**, A51
- De Grandi S., et al., 1999, *ApJ*, **514**, 148
- Di Gennaro G., et al., 2021, *Nature Astronomy*, **5**, 268
- Duchesne S., 2021, Data for an MWA-2 survey of diffuse radio emission in galaxy clusters, [doi:10.26185/611f33b774e96](https://doi.org/10.26185/611f33b774e96), <https://dx.doi.org/10.26185/611f33b774e96>
- Duchesne S. W., Johnston-Hollitt M., Zhu Z., Wayth R. B., Line J. L. B., 2020, *PASA*, **37**, e037
- Duchesne S. W., Johnston-Hollitt M., Bartalucci I., Hodgson T., Pratt G. W., 2021a, *PASA*, **38**, e005
- Duchesne S. W., Johnston-Hollitt M., Offringa A. R., Pratt G. W., Zheng Q., Dehghan S., 2021b, *PASA*, **38**, e010
- Duchesne S. W., Johnston-Hollitt M., Wilber A. G., 2021c, *PASA*, **38**, e031
- Duffy P., Blundell K. M., 2012, *MNRAS*, **421**, 108
- Dwarakanath K. S., Parekh V., Kale R., George L. T., 2018, *MNRAS*, **477**, 957
- Enßlin T. A., Brüggen M., 2002, *MNRAS*, **331**, 1011
- Enßlin T. A., Gopal-Krishna 2001, *A&A*, **366**, 26
- Enßlin T. A., Biermann P. L., Klein U., Kohle S., 1998, *A&A*, **332**, 395
- Fairall A. P., 1984, *MNRAS*, **210**, 69
- Finoguenov A., Sarazin C. L., Nakazawa K., Wik D. R., Clarke T. E., 2010, *ApJ*, **715**, 1143
- Flaugher B., et al., 2015, *AJ*, **150**, 150
- Fleener M. C., Rose J. A., Christiansen W. A., Johnston-Hollitt M., Hunstead R. W., Drinkwater M. J., Saunders W., 2006, *AJ*, **131**, 1280
- Flin P., Krywult J., 2006, *A&A*, **450**, 9
- Fruscione A., et al., 2006, in Proc. SPIE. p. 62701V, [doi:10.1117/12.671760](https://doi.org/10.1117/12.671760)
- Garilli B., Maccagni D., Tarengchi M., 1993, *A&AS*, **100**, 33
- Garmire G. P., Bautz M. W., Ford P. G., Nousek J. A., Ricker George R. J., 2003, in Truemper J. E., Tananbaum H. D., eds, Society of Photo-Optical Instrumentation Engineers (SPIE) Conference Series Vol. 4851, X-Ray and Gamma-Ray Telescopes and Instruments for Astronomy. pp 28–44, [doi:10.1117/12.461599](https://doi.org/10.1117/12.461599)
- Giacintucci S., Markevitch M., Cassano R., Venturi T., Clarke T. E., Kale R., Cuciti V., 2019, *ApJ*, **880**, 70
- Giacintucci S., Markevitch M., Johnston-Hollitt M., Wik D. R., Wang Q. H. S., Clarke T. E., 2020, *ApJ*, **891**, 1
- Gitti M., Brunetti G., Setti G., 2002, *A&A*, **386**, 456
- Golovich N., et al., 2019, *ApJ*, **882**, 69
- Govoni F., et al., 2019, *Science*, **364**, 981
- Hambly N. C., et al., 2001a, *MNRAS*, **326**, 1279
- Hambly N. C., Irwin M. J., MacGillivray H. T., 2001b, *MNRAS*, **326**, 1295
- Hambly N. C., Davenhall A. C., Irwin M. J., MacGillivray H. T., 2001c, *MNRAS*, **326**, 1315
- Hancock P. J., Trott C. M., Hurley-Walker N., 2018, *PASA*, **35**, e011
- Hardcastle M. J., Sakelliou I., 2004, *MNRAS*, **349**, 560
- Hindson L., et al., 2014, *MNRAS*, **445**, 330
- Hodgson T., Johnston-Hollitt M., McKinley B., Vernstrom T., Vacca V., 2020, *PASA*, **37**, e032
- Hodgson T., Bartalucci I., Johnston-Hollitt M., McKinley B., Vazza F., Wittor D., 2021, *ApJ*, **909**, 198
- Hoefl M., Brüggen M., 2007, *MNRAS*, **375**, 77
- Hota A., et al., 2011, *MNRAS*, **417**, L36
- Hotan A., McConnell D., Whiting M., Huynh M., 2020b, ASKAP Data Products for Project AS110 (The Rapid ASKAP Continuum Survey): images and visibilities. v1. CSIRO. Data Collection, <http://hdl.handle.net/102.100.100/374841?index=1>
- Hotan A., Whiting M., Huynh M., Moss V., 2020a, ASKAP Data Products for Project AS113 (Other ASKAP pilot science including tests, TOO or guest observations): images and visibilities. v1. CSIRO. Data Collection., <http://hdl.handle.net/102.100.100/348894?index=1>
- Hotan A. W., et al., 2021, *PASA*, **38**, e009
- Hunter J. D., 2007, *Computing in Science and Engineering*, **9**, 90
- Hurley-Walker N., et al., 2017, *MNRAS*, **464**, 1146
- Huynh M., Dempsey J., Whiting M. T., Ophel M., 2020, in Ballester P., Ibsen J., Solar M., Shortridge K., eds, Astronomical Society of the Pacific Conference Series Vol. 522, Astronomical Data Analysis Software and Systems XXVII. p. 263
- Intema H. T., Jagannathan P., Mooley K. P., Frail D. A., 2017, *A&A*, **598**, A78
- Jaffe W. J., 1977, *ApJ*, **212**, 1
- Johnston-Hollitt M., 2003, PhD thesis, University of Adelaide
- Jonas J., MeerKAT Team 2016, in MeerKAT Science: On the Pathway to the SKA. p. 1

- Jones E., Oliphant T., Peterson P., et al., 2001, SciPy: Open source scientific tools for Python, <http://www.scipy.org/>
- Jones D. H., et al., 2009, *MNRAS*, 399, 683
- Jurlin N., et al., 2020, *A&A*, 638, A34
- Kang H., 2015, *Journal of Korean Astronomical Society*, 48, 155
- Kang H., 2018, *Journal of Korean Astronomical Society*, 51, 185
- Kang H., Ryu D., 2011, *ApJ*, 734, 18
- Kang H., Ryu D., 2016, *ApJ*, 823, 13
- Kempner J. C., Sarazin C. L., 2001, *ApJ*, 548, 639
- Knowles K., et al., 2021, *MNRAS*, 504, 1749
- Line J. L. B., Webster R. L., Pindor B., Mitchell D. A., Trott C. M., 2017, *PASA*, 34, e003
- Loi F., et al., 2017, *MNRAS*, 472, 3605
- Lovisari L., et al., 2017, *ApJ*, 846, 51
- Macario G., Venturi T., Brunetti G., Dallacasa D., Giacintucci S., Cassano R., Bardelli S., Athreya R., 2010, *A&A*, 517, A43
- Macario G., et al., 2013, *A&A*, 551, A141
- Mahatma V. H., et al., 2018, *MNRAS*, 475, 4557
- Mandal S., et al., 2020, *A&A*, 634, A4
- Markevitch M., Govoni F., Brunetti G., Jerius D., 2005, *ApJ*, 627, 733
- Mauch T., Murphy T., Buttery H. J., Curran J., Hunstead R. W., Piestrzynski B., Robertson J. G., Sadler E. M., 2003, *MNRAS*, 342, 1117
- McConnell D., et al., 2020, *PASA*, 37, e048
- Morganson E., et al., 2018, *PASP*, 130, 074501
- Murgia M., Govoni F., Markevitch M., Feretti L., Giovannini G., Taylor G. B., Carretti E., 2009, *A&A*, 499, 679
- Murgia M., et al., 2011, *A&A*, 526, A148
- Murphy T., Mauch T., Green A., Hunstead R. W., Piestrzynska B., Kels A. P., Sztajer P., 2007, *MNRAS*, 382, 382
- Murphy T., et al., 2013, *PASA*, 30, e006
- Murphy T., Lenc E., Whiting M., Huynh M., Hotan A., 2019, ASKAP Data Products for Project AS111 (ASKAP Pilot Survey for Gravitational Wave Counterparts): images and visibilities. v1. CSIRO. Data Collection, <http://hdl.handle.net/102.100.100/175570?index=1>
- Murphy T., et al., 2020, ASKAP Data Products for Project AS107 (ASKAP Pilot Survey for VAST): images and visibilities. v1. CSIRO. Data Collection, <http://hdl.handle.net/102.100.100/340961?index=1>
- Nuza S. E., Hoeft M., van Weeren R. J., Gottlöber S., Yepes G., 2012, *MNRAS*, 420, 2006
- Ochsenbein F., Bauer P., Marcout J., 2000, *A&AS*, 143, 23
- Offringa A. R., Smirnov O., 2017, *MNRAS*, 471, 301
- Offringa A. R., et al., 2014, *MNRAS*, 444, 606
- Offringa A. R., et al., 2015, *PASA*, 32, e008
- Offringa A. R., et al., 2016, *MNRAS*, 458, 1057
- Ogrean G. A., et al., 2015, *ApJ*, 812, 153
- Orrù E., Murgia M., Feretti L., Govoni F., Brunetti G., Giovannini G., Girardi M., Setti G., 2007, *A&A*, 467, 943
- Parma P., Murgia M., de Ruiter H. R., Fanti R., Mack K. H., Govoni F., 2007, *A&A*, 470, 875
- Pearce C. J. J., et al., 2017, *ApJ*, 845, 81
- Piffaretti R., Arnaud M., Pratt G. W., Pointecouteau E., Melin J.-B., 2011, *A&A*, 534, A109
- Planck Collaboration et al., 2014, *A&A*, 571, A29
- Planck Collaboration et al., 2015, *A&A*, 581, A14
- Planck Collaboration et al., 2016, *A&A*, 594, A27
- Poole G. B., Fardal M. A., Babul A., McCarthy I. G., Quinn T., Wadsley J., 2006, *MNRAS*, 373, 881
- Pratt G. W., Croston J. H., Arnaud M., Böhringer H., 2009, *A&A*, 498, 361
- Quici B., et al., 2021, *PASA*, 38, e008
- Rajpurohit K., et al., 2020, *A&A*, 642, L13
- Rajpurohit K., et al., 2021a, arXiv e-prints, p. arXiv:2104.05690
- Rajpurohit K., et al., 2021b, *A&A*, 646, A56
- Rajpurohit K., et al., 2021c, *A&A*, 646, A135
- Richard-Laferrrière A., et al., 2020, *MNRAS*, 499, 2934
- Robitaille T., Bressert E., 2012, APLpy: Astronomical Plotting Library in Python, Astrophysics Source Code Library (ascl:1208.017)
- Rossetti M., Gastaldello F., Eckert D., Della Torre M., Pantiri G., Cazzoletti P., Molendi S., 2017, *MNRAS*, 468, 1917
- Sakelliou I., Hardcastle M. J., Jetha N. N., 2008, *MNRAS*, 384, 87
- Santos J. S., Rosati P., Tozzi P., Böhringer H., Ettori S., Bignamini A., 2008, *A&A*, 483, 35
- Schwöpe A., et al., 2000, *Astronomische Nachrichten*, 321, 1
- Slee O. B., Roy A. L., Murgia M., Andernach H., Ehle M., 2001, *AJ*, 122, 1172
- Struble M. F., Rood H. J., 1999, *ApJS*, 125, 35
- Strüder L., et al., 2001, *A&A*, 365, L18
- Subrahmanyan R., Ekers R. D., Saripalli L., Sadler E. M., 2010, *MNRAS*, 402, 2792
- Tarrio P., Melin J. B., Arnaud M., Pratt G. W., 2016, *A&A*, 591, A39
- Tarrio P., Melin J. B., Arnaud M., 2018, *A&A*, 614, A82
- Thierbach M., Klein U., Wielebinski R., 2003, *A&A*, 397, 53
- Thorat K., Subrahmanyan R., Saripalli L., Ekers R. D., 2013, *ApJ*, 762, 16
- Tingay S. J., et al., 2013, *PASA*, 30, 7
- Tonry J. L., et al., 2012, *ApJ*, 750, 99
- Trasatti M., Akamatsu H., Lovisari L., Klein U., Bonafede A., Brügger M., Dallacasa D., Clarke T., 2015, *A&A*, 575, A45
- Turner M. J. L., et al., 2001, *A&A*, 365, L27
- Urdampilleta I., Simionescu A., Kaastra J. S., Zhang X., Di Gennaro G., Mernier F., de Plaa J., Brunetti G., 2021, *A&A*, 646, A95
- Vazza F., Wittor D., Brunetti G., Brügger M., 2021, arXiv e-prints, p. arXiv:2102.04193
- Venturi T., Giacintucci S., Dallacasa D., Cassano R., Brunetti G., Bardelli S., Setti G., 2008, *A&A*, 484, 327
- Vikhlinin A., McNamara B. R., Forman W., Jones C., Quintana H., Hornstrup A., 1998, *ApJ*, 502, 558
- Voges W., et al., 1999, *A&A*, 349, 389
- Wayth R. B., et al., 2015, *PASA*, 32, 25
- Wayth R. B., et al., 2018, *PASA*, 35
- Wen Z. L., Han J. L., 2015, *ApJ*, 807, 178
- Wen Z. L., Han J. L., Liu F. S., 2012, *ApJS*, 199, 34
- Wilber A., et al., 2018, *MNRAS*, 473, 3536
- Wilber A., et al., 2019, *A&A*, 622, A25
- Wilber A. G., Johnston-Hollitt M., Duchesne S. W., Tasse C., Akamatsu H., Intema H., Hodgson T., 2020, *PASA*, 37, e040
- Xie C., et al., 2020, *A&A*, 636, A3
- Zaritsky D., Gonzalez A. H., Zabludoff A. I., 2006, *ApJ*, 638, 725
- de Gasperin F., 2017, *MNRAS*, 467, 2234
- de Gasperin F., van Weeren R. J., Brügger M., Vazza F., Bonafede A., Intema H. T., 2014, *MNRAS*, 444, 3130
- de Gasperin F., Intema H. T., van Weeren R. J., Dawson W. A., Golovich N., Wittman D., Bonafede A., Brügger M., 2015, *MNRAS*, 453, 3483
- de Gasperin F., et al., 2017, *Science Advances*, 3, e1701634
- van Haarlem M. P., et al., 2013, *A&A*, 556, A2
- van Weeren R. J., Röttgering H. J. A., Brügger M., Hoeft M., 2010, *Science*, 330, 347
- van Weeren R. J., Brügger M., Röttgering H. J. A., Hoeft M., Nuza S. E., Intema H. T., 2011, *A&A*, 533, A35
- van Weeren R. J., Röttgering H. J. A., Intema H. T., Rudnick L., Brügger M., Hoeft M., Oonk J. B. R., 2012, *A&A*, 546, A124
- van Weeren R. J., et al., 2016, *ApJ*, 818, 204
- van Weeren R. J., et al., 2017, *Nature Astronomy*, 1, 0005
- van Weeren R. J., de Gasperin F., Akamatsu H., Brügger M., Feretti L., Kang H., Stroe A., Zandanel F., 2019, *Space Sci. Rev.*, 215, 16
- van Weeren R. J., et al., 2021, *A&A*, 651, A115
- van der Walt S., Colbert S. C., Varoquaux G., 2011, *Computing in Science Engineering*, 13, 22

A. Non-candidates

In this section we will record clusters previously reported as having candidate diffuse emission by D21 but are shown by the MWA-2 data to be discrete sources. Note that while FIELD1 and FIELD2

overlap with a majority image used by Duchesne et al. 2021b, for some clusters towards the edges of the fields we are unable to confirm the presence of either diffuse emission or discrete sources—these clusters are not mentioned here.

Abell 0022. Edge of image. Inconclusive.

Abell 0033. Edge of image. Inconclusive.

Abell 2798. Resolution still not sufficient. Inconclusive.

Abell S1136. To be discussed in Macgregor et al. (in prepatation).

Abell S1063. Halo reported by Xie et al. (2020).

Abell 2556. The MWA-2 216-MHz, robust +0.5 image breaks up into three discrete point sources. RACS data confirm the source is a number of point sources and a double-lobed radio galaxy, with a spectral index $\alpha \sim -0.8$. The steeper spectral index reported by D21 is a result of point sources contributing to the 168-MHz measurement but not the 1.4-GHz measurement.

Abell S0084. MWA-2 data breaks into two discrete components and RACS confirms this. We cannot confirm the candidate halo/mini-halo.

Abell S1121. Out of images.

PSZ G082.31–67.01. Out of images.

B. Measured source properties

A table of measured and derived source properties are provided for all frequencies (88, 118, 154, 169, 185, 200, 216, 887, 943, and 1400 MHz, though note not all sources are measured at every frequency) as supplementary online material available at the data store for the Publications of the Astronomical Society of Australia, hosted at <https://data-portal.hpc.swin.edu.au/institute/pasa> (Duchesne, 2021)²⁶. The following details the columns available for each source:

- C0 `cluster_name`
Name of cluster as it appears in Table 1.
- C1 `source_id`
ID of source as used in Section 3.1 and in figures.
- C2 `flux_$nu` (mJy)
Final flux density of source at frequency \$nu MHz.
- C3 `err_flux_$nu` (mJy)
Uncertainty on the final flux density of source at frequency \$nu MHz.
- C4 `conf_$nu` (mJy)
Total confusing flux density subtracted from initial measurement at frequency \$nu MHz.
- C5 `err_conf_$nu` (mJy)
Uncertainty on total confusing flux density subtracted from initial measurement at frequency \$nu MHz. This is added in quadrature to the initial measurement.
- C6 `psf_a_$nu` (arcsec)
FWHM of PSF major axis in \$nu-MHz image at the source location.
- C7 `psf_b_$nu` (arcsec)
FWHM of PSF minor axis in \$nu-MHz image at the source location.

⋮

C56 `alpha_mwa`

Spectral index across the MWA-2 images as shown in Fig. 26(i)–(xxix).

C57 `alpha`

Spectral index across all data for power law models as shown in Fig. 26(i)–(xxix).

C58 `q`

Curvature parameter for curved power law model fits (Eq. 6), as shown in Fig. 26(i)–(xxix).

C. Integrated spectra

Fig. 26(i)–(xxix) show the SEDs for all sources reported in Section 3.1. For each source with MWA-2 and additional data, we additionally provide a power law fit to the MWA-2 data only.

D. Flux recovery in MWA-2 data

Fig. 27(i)–(ix) show the ratios of dirty to CLEAN flux density for Gaussian models of varying FWHM. For each source the residual flux density is integrated and multiplied by the factor $S_{\text{CLEAN}}/S_{\text{dirty}}$ to account for this. Additional detail of this process is provided in Duchesne et al. (2021c).

²⁶<https://dx.doi.org/10.26185/611f33b774e96>

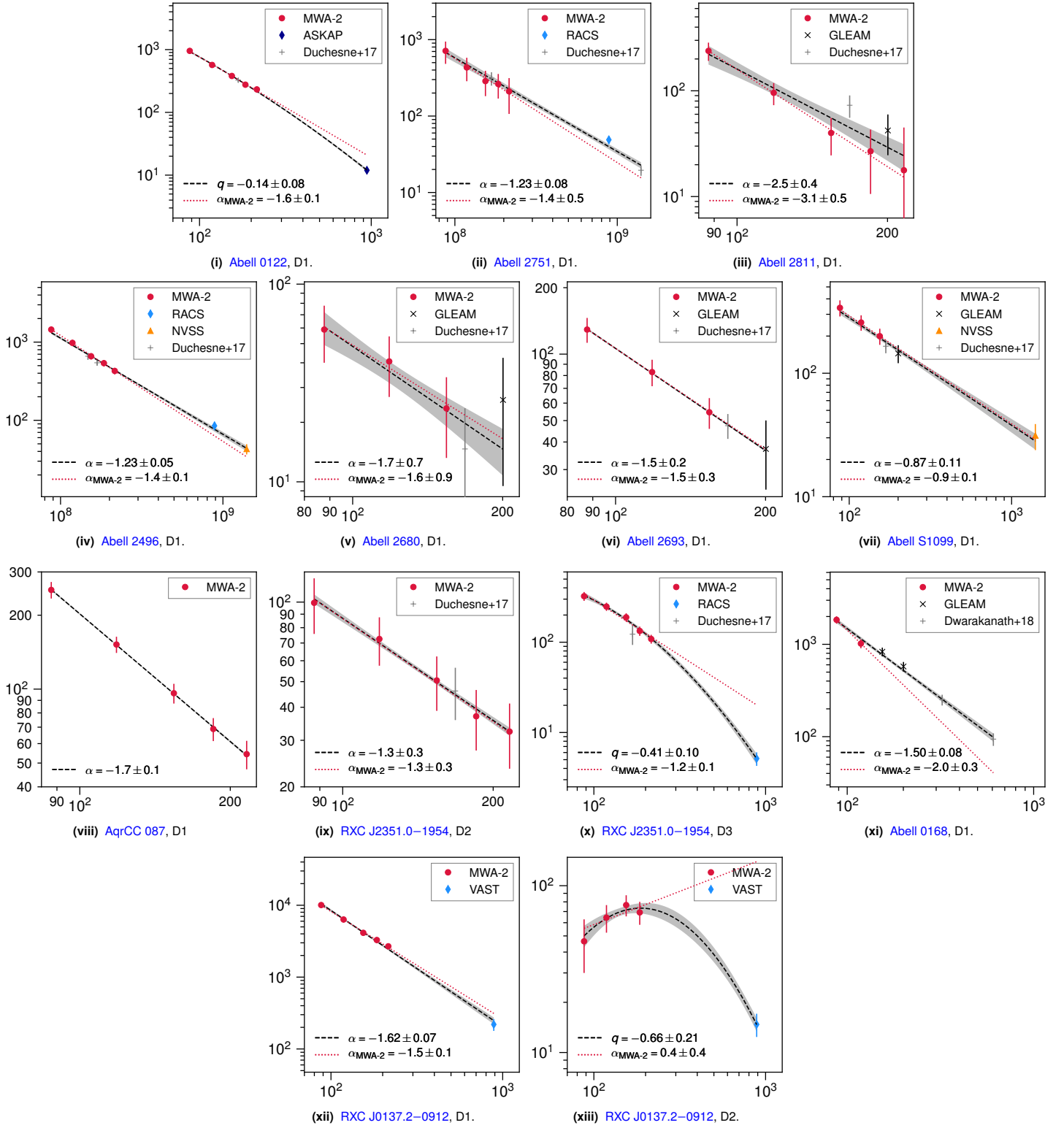


Figure 26. Integrated spectra of diffuse sources described in Section 3.1 in the order they are reported. The ordinate and abscissa are integrated flux density (mJy) and frequency (MHz), respectively. Individual measurements are reported in the online table described in Appendix B. The dashed, black lines are the fits for the full set of measurements (with grey, shaded regions corresponding to 95% confidence intervals) and the red, dotted lines are fits for only the MWA-2 data. Note black arrows represent limits. Note if only two data points are available, a two-point spectral index was calculated and the resultant line is drawn based on that spectral index. For curved power law spectra, we report the curvature, q , rather than the equivalent spectral index.

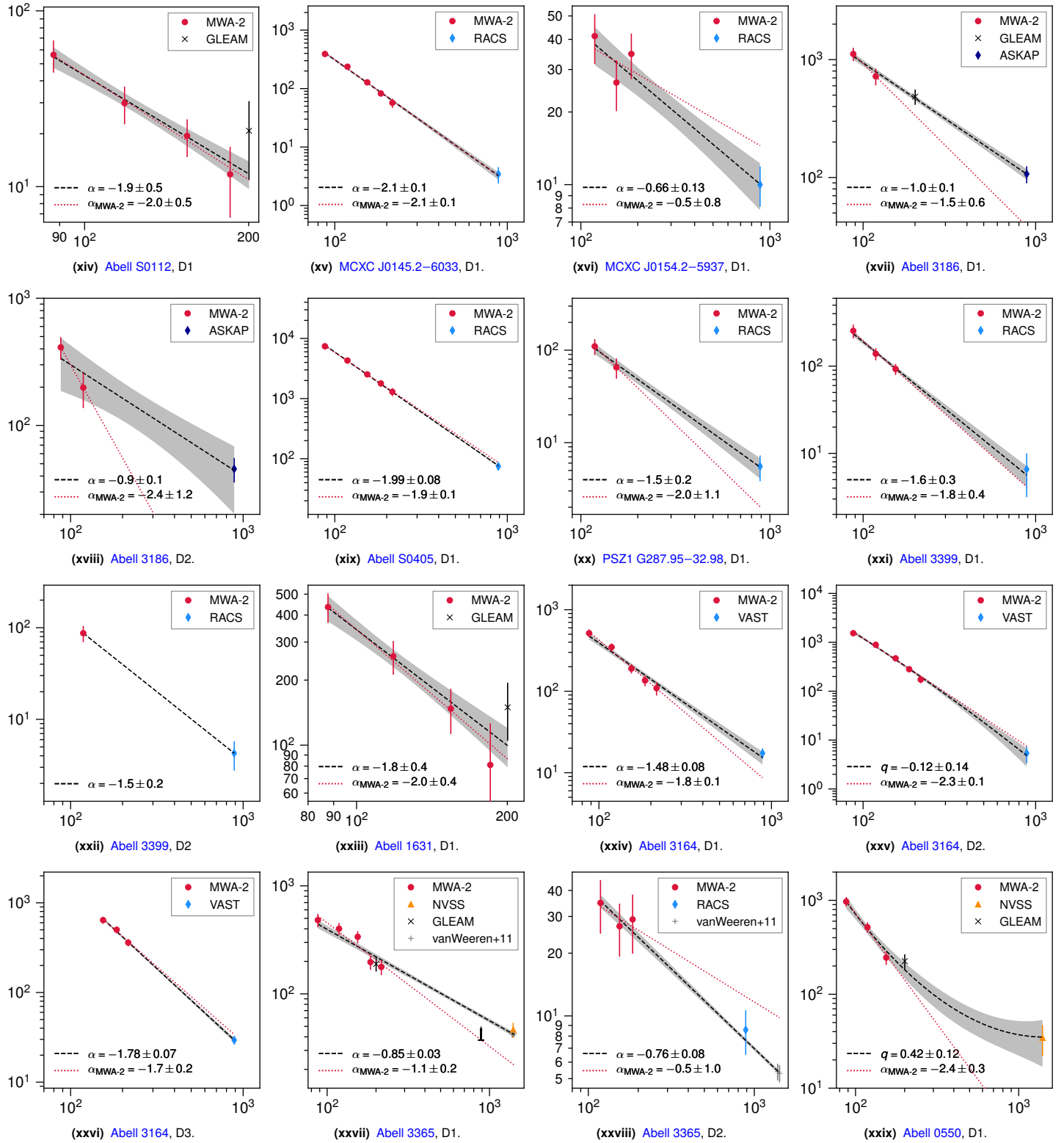


Figure 26. continued.

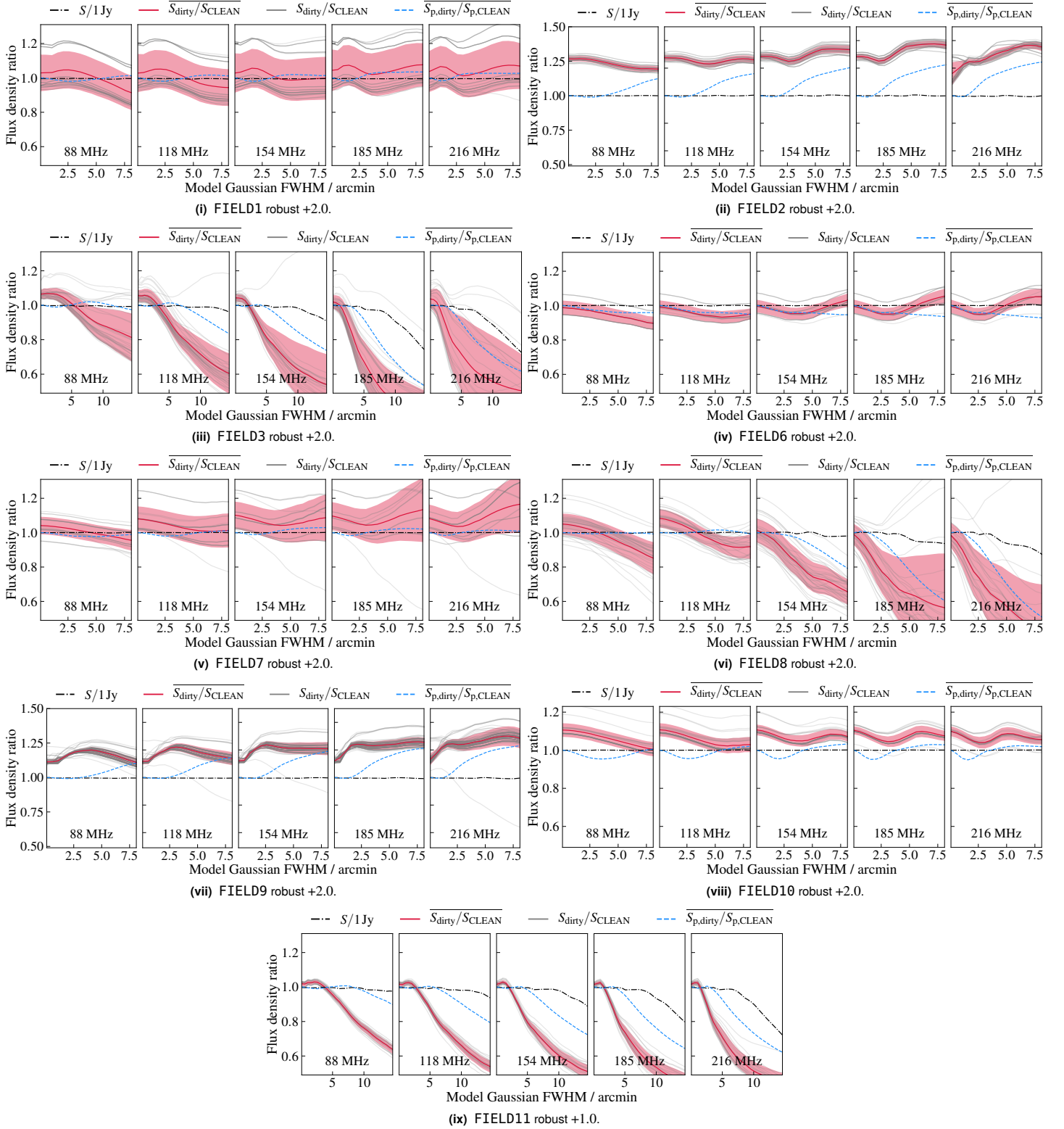


Figure 27. Flux recovery and ratio of deconvolved ('CLEAN') to un-deconvolved ('dirty') integrated flux density for individual snapshots (grey lines). The angular scale on the abscissa correspond to FWHM of the simulated Gaussian (sampled every 30 arcsec). The mean profile, $\overline{S_{dirty}/S_{CLEAN}}$, is plotted with the standard deviation plotted as a red shaded region. The mean peak flux profile, $\overline{S_{p,dirty}/S_{p,CLEAN}}$, is also shown. (i) and (vi) are re-produced from Duchesne et al. (2021c) for completeness.